FACULTY OF SCIENCE AND ENGINEERING

IEM MASTER DESIGN PROJECT

MASTER INTERNSHIP

Behavior and influence of inert gas flow during selective laser melting

Author
David Veninga

Student Number:
S2994801

First supervisor
Second supervisor
Company supervisor

Dr. M. Muñoz-Arias
Prof. Dr. Y. Pei
Dr. T.C. Pijper (Philips)

March 25, 2021

Abstract

Selective laser melting (SLM) is an innovative additive manufacturing (AM) process capable of fabricating metal parts through addition of material. The technique, in which a high-power laser selectively scans and melts areas of a metal powder bed, offers great advantages in manufacturing complex parts at a high material utilization rate with freedom of design. During the SLM process, an inert gas is fed through the build chamber to create an inert atmosphere, and to transport unfavorable process by-products away from the laser beam and powder bed. Advanced Additive (ICD-AM), a project of the Innovation Cluster Drachten (ICD), investigates SLM's potential within the stakeholders' companies. Currently, they lack sufficient knowledge of the argon gas flow behavior and influence in their SLM 280HL process. This Master Design project (MDP) investigated the argon gas flow behavior and influence in the SLM 280HL process through measurements, simulations, and experiments. Gas flow behavior in front of the inlet and over the build plate was found to be nonuniform, in contrast to what was previously assumed within ICD-AM. Evaluation of 316L stainless steel experimental batches printed at different flow velocities (default flow velocity and 67% of default flow velocity) revealed significant differences in surface roughness, microstructure and porosity of the samples. The influence of inert gas flow velocity on surface roughness was further confirmed through regression analysis, in which a statistically significant correlation was found between the measured gas flow profile and the surface roughness distribution over the build plate. A very high degree of lack of fusion was discovered in the samples printed at lower gas flow velocity, an observation which could be well-connected to gas flow-related mechanisms such as beam attenuation and redeposition. All results obtained in the project were validated through statistical analysis. Compared to other process parameters, the inert gas flow velocity during the SLM process has been relatively overlooked in existing literature. The experimental results of this project confirm the significant influence of inert gas flow on quality metrics of the SLM process: surface roughness and microstructure, and porosity.

Contents

Nomenclature

AM	Additive manufacturing
ANOVA	Analysis of variance
CAD	Computer-aided design
CFD	Computational fluid dynamics
DOF	Degree of freedom
HWA	Hot-wire anemometry
ICD	Innovation Cluster Drachten
ICD-AM	Advanced Additive project
LBM	Laser beam melting
LOF	Lack of fusion
MAPE	Mean average percentage error
MDP	Master Design project
SEM	Scanning electron microscope
SLM	Selective laser melting
SMART	Specific, measurable, achievable, relevant, timely

1   Introduction

Additive manufacturing (AM), also known as 3D printing, is a relatively novel manufacturing method indicating the production of parts in a layer-by-layer fashion [1]. Characteristic for the AM technique is the production of parts through addition of material, in contrast to conventional, subtractive methods. AM offers benefits such as freedom of design, waste minimization and flexible production [2]. Due to these unique advantages, AM has been widely applied in varying industries, such as aerospace, medical devices, military and automotive [3, 4, 5].
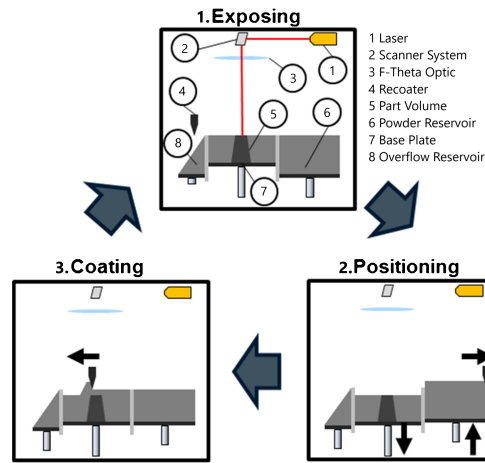
Figure 1: Schematic overview of the three main SLM process steps: 1) Laser melting of part layer, 2) Lowering of build platform and positioning of recoater, 3) Deposition of new powder layer by the recoater. [6]

Selective laser melting (SLM) is an AM process capable of fabricating metal parts, in which a high-power density laser selectively scans and melts areas of a metal powder bed [7]. Prior to the SLM process, the CAD file of the final part is sliced into layers, which are further decomposed into laser scan paths. Each layer is processed in sequence according to the SLM process cycle in Figure 1, which is continued until the completion of all layers. A detailed description of the SLM process is provided in Section 2.3. SLM offers a great advantage in manufacturing complex parts at a high material utilization rate [8]. Despite its obvious potential, and the method being relatively mature [9], repeatability and reproducibility remain critical issues impeding the widespread implementation of SLM in industry [10].

1.1   Problem context

The Innovation Cluster Drachten (ICD) is a collaboration between high-tech companies in an around the city of Drachten. They are at the forefront of technical innovations in products and solutions worldwide. One of their projects, Advanced Additive (ICD-AM), investigates how 3D-printing can be applied within the partners' organizations. SLM is one of the main focal points of the ICD-AM project.

One open question of ICD-AM regarding the SLM process concerns the inert gas flow in the SLM 280HL printer, an SLM system produced by SLM Solutions and procured by the ICD for the purpose of R&D. To maintain an inert atmosphere during the SLM process and to remove process by-products such as vapors and spatter, an inert gas (argon) is fed through the build chamber. Previous studies have confirmed that the inert gas affects various quality parameters of the final SLM-manufactured part, such as porosity [6, 11, 12] and mechanical properties [11, 13, 14]. Currently, the ICD-AM group has insufficient knowledge of inert gas flow behavior in the SLM 280HL and inert gas flow influence on build quality. Therefore, this Master Design project (MDP) has been requested by ICD-AM in order to bridge this knowledge gap.

2 Problem analysis

The problem underlying this project regards the limited knowledge of the ICD-AM group concerning the inert gas flow in the SLM 280HL. As stated by Ladewig et al. [6], the inert argon flow through the build chamber has two main functions:

1. To maintain an inert atmosphere with low oxygen levels ($<0.1\%$) during the SLM process, to prevent chemical reactions such as oxidation. Oxidation in the final microstructure may lead to defects.

2. To transport unfavorable process by-products (Figure 5), such as smoke and spatter, away from the laser beam and powder bed. Insufficient removal may lead to beam attenuation (interference of by-products with laser beam) and redeposition of ejected powder and spatter, which may lead to lack of fusion (LOF) defects, which are shown in Figure 2. LOF defects arise when the laser does not deliver enough energy in the melt pool to fuse the molten layer to the previous layer [6].
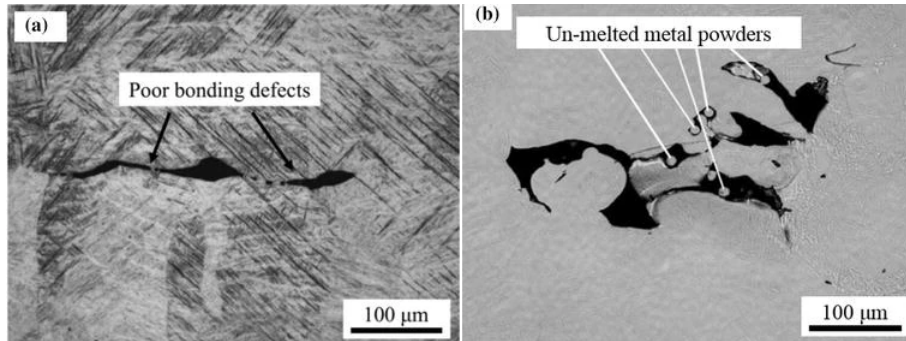
Figure 2: Optical images of LOF defects in SLM fabricated parts: (a) Poor bonding defects; (b) LOF defects with unmelted metal powders [7]. [15]

Apart from aforementioned functions, the inert gas flow also influences the SLM process through convective cooling of the melt pool:

3. A third influence of the argon gas flow on the SLM process is through convective heat transfer. Heat from the melt pool is transferred to the argon flowing over the melt pool through convection, cooling the melt pool. Higher inert gas flow velocity increases the heat transferred from the melt pool through convection, as confirmed by Spears & Gold [16].

Aforementioned influences of the inert gas flow on the SLM process are further elaborated in Section 2.2. In-depth study of literature concluded that gas-related

process parameters influence material properties of SLM-manufactured parts, such as porosity [6, 11, 12], surface morphology [6], microstructure [6, 14] and mechanical properties [11, 13, 14]. Furthermore, it is hypothesized that parameters such as residual stresses and surface roughness are also affected by gas flow, however, literature on these topics is limited. Some preliminary tests with varying gas flow velocities conducted within the ICD-AM group confirmed the influence of gas flow velocity on at least the surface morphology and microstructure of the SLM-manufactured parts.

2.1 Stakeholder analysis

This MDP was commissioned by ICD-AM to bridge their knowledge gap concerning the inert gas flow during the SLM process. They are defined as a key player in this project. Dr. T.C. Pijper, project lead of ICD-AM, is the problem owner in this project. ICD-AM's requirements for the project can be summarized into the following requirements:

- To gain a thorough understanding of the gas flow behavior in the build chamber and close to the powder bed.

- To evaluate the influence of inert gas flow on printing quality of the SLM 280HL.

Furthermore, three companies are included in the project as stakeholders: Philips, NTS-Norma and Stork. These three companies are actively involved in the ICD-AM project to investigate the potential of SLM in applications in their respective companies. SLM's potential for Philips lies in the manufacturing of tools and robot arm parts, as well as rapid prototyping. NTS-Norma and Stork consider SLM as a potential manufacturing method for end products. Therefore, certification of SLM as a fabrication method for end products is of concern for NTS-Norma and Stork. Understanding gas flow behavior and influence in the SLM 280HL may contribute to this goal. Otherwise, the requirements for the MDP from these three companies are similar to ICD-AM's requirements. All project stakeholders and their interest and influence in the project are shown in Figure 3.
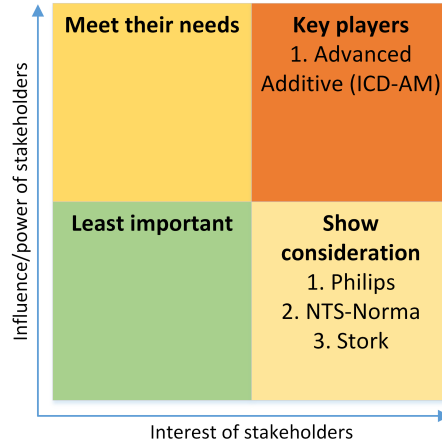
Figure 3: Stakeholder matrix showing position of stakeholders in project. Adapted from Johnson & Scholes [17].

The term *printing quality* stated in the stakeholders' requirements should be specified to fit inside the timeframe of this MDP. Therefore, a choice of material properties to evaluate was made in consultation with the project's stakeholders. This is covered in Section 2.3.

2.2 Literature review: Influence of inert gas flow during the SLM process

Earlier in this report, three main influences of the inert gas flow on the SLM process were defined: creation of an inert atmosphere, transport of unfavorable process by-products, and convective cooling of the laser melt pool. An in-depth literature study was conducted to gain a deeper understanding of these three mechanisms and their influence on SLM-manufactured parts.

2.2.1 Inert atmosphere during SLM process

One of the main functions of the inert gas flow is to create an inert, low-oxygen atmosphere to prevent chemical reactions such as oxidation. When the laser beam melts the powder bed, the temperature of the powder bed is increased significantly and the formation of stable oxides is likely to occur [18]. Velasco-Castro et al. [19] investigated the effects of oxygen pickup during SLM on the microstructure and mechanical properties of Ti-6Al-4V lattices. They concluded that higher oxygen levels led to significantly reduced ductility and compression strength. Li et al. [20] found that balling, a typical SLM defect, was significantly influenced by the oxygen content present in the inert atmosphere. During SLM, the laser molten track possesses a

shrinking tendency through surface tension, therefore balling is easily formed during the SLM process. Big-size balling is detrimental to both the SLM process and the quality of the final parts, as it may induce porosity in the microstructure and a coarse surface. Furthermore, the uniform distribution of a fresh powder layer may be disrupted by big-sized balling in the previous layer. Figure 4 shows SEM images of balling characteristics at different atmosphere oxygen levels.
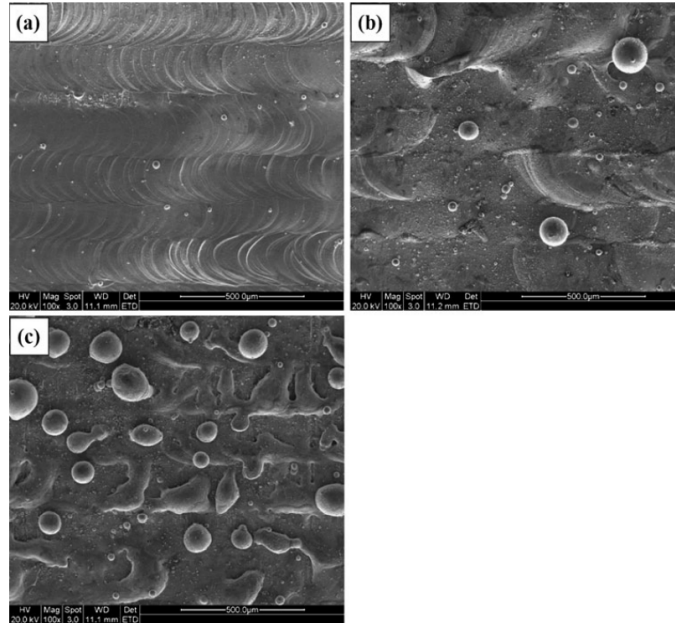
Figure 4: SEM image showing balling characteristics under different oxygen contents in atmosphere: a) 0.1 % b) 2 % c) 10 %. [20]

2.2.2 Transport of process by-products

The second main function of the inert gas flow is the transport of unfavorable process by-products which are produced during the SLM process. To understand the influence of process by-products on part quality, it is important to understand their formation and influence on the SLM process. Figure 5 shows a schematic overview of possible by-products during SLM.

Figure 5: Schematic overview of possible by-products during SLM [6].

2.2.2.1 Formation of process by-products during SLM

In Figure 5, two categories of process by-products can be distinguished: the welding plume, and spatter and ejected powder.

The welding plume consists of two by-products: a plasma plume, and metal vapor. The interaction of the high power-density laser and the metal powder bed can cause the gas directly above the interaction zone to become ionized, forming the plasma plume [6]. In addition to plasma, metal vapor is also present in the welding plume, due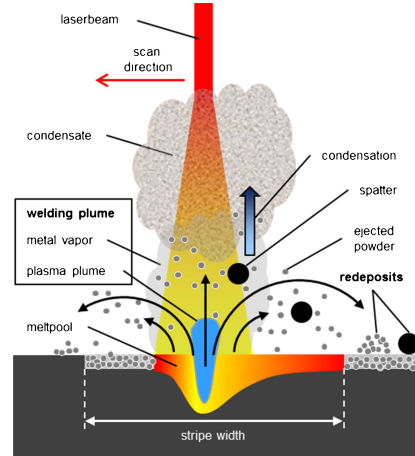 to alloying elements in the laser spot evaporating. Rapid cooling of the vaporized elements forms particles. Noskov et al. [21] studied these ultrafine particles, and found that they were mainly spherical in shape and consisted of alloying oxides, whereas larger particles (>30 nm diameter) were characterized by a metallic core and an oxide surface layer.

The other types of process by-products established through the SLM process are spatter and ejected powder. Spatter, liquid metal particles ejected from the melt pool during welding, can be formed during the SLM process by volatile alloying elements or instabilities in the melt pool [6]. Lutter-Günther et al. [22] defined three types of spatter and ejected powder: blown away powder, spherical spatter and agglomerated spatter. The different spatter types are shown in Figure 6. Blown away (ejected) powder indicates unmelted powder particles close to the melt pool which are expelled through the pressure generated by the melt pool and welding plume. Spherical spatter indicates spatter ejected from the melt pool under a high angle, giving the spatter sufficient time to solidify while in flight. Spherical spatter typically forms a thick oxide surface layer. Agglomerated spatter indicates molten droplets ejected from the melt pool under a low angle. The droplets lack sufficient
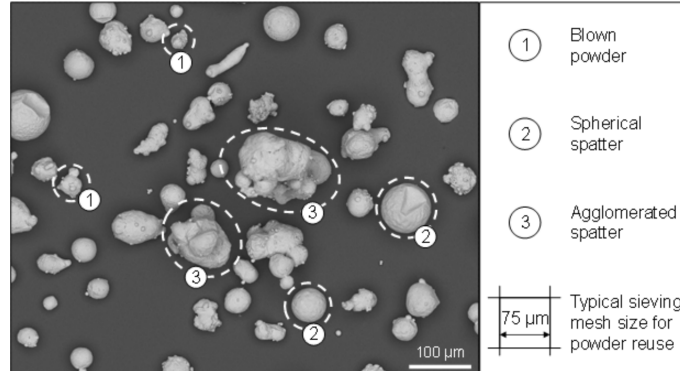
Figure 6: SEM image of collected spatter particles from LBM processing of AlSi10Mg powder. [22]

time to solidify before colliding with the powder bed. Therefore, the liquified spatter wets multiple powder particles and forms a large, irregularly shaped agglomerate. Simoncelli et al. [23] concluded that the chemical composition of spatter is similar to that of virgin powder. Based on their findings, Ladewig et al. [6] suggested that the spatter is formed as a result of melt pool instabilities, rather than vaporization effects.

2.2.2.2 Influence of process by-products on SLM process

Both types of process by-products previously discussed can affect the SLM process. The two main mechanisms through which this happens are beam attenuation and redeposition.

Beam attenuation indicates the loss of laser beam intensity through interference of process by-products. Beam attenuation includes multiple mechanisms, such as laser power absorption by process by-products, laser reflection and laser beam scattering. When present in the laser path, all aforementioned by-products can lead to beam attenuation [6]. Attenuation of the beam leads to lower power in the melt pool, which may lead to insufficient fusion to the previous layer. Previous research by Shchleglov et al. [24] and Greses et al. [25] presented maximum values of beam attenuation of 40%, which can certainly lead to LOF defects. Grünberger & Domröse [26] investigated beam attenuation in SLM. Their findings were that the mechanism occurs randomly, and that the probability that beam attenuation occurs is related to the gas flow rate. Lower gas flow rate leads to less effective removal of process by-products, therefore increasing the probability of beam attenuation.

Redeposition is another mechanism through which process by-products may influence the SLM process. Spatter and ejected powder, as well as condensed powder

ejected from the melt pool, can be deposited elsewhere on the build plate. This may be somewhere on the fresh powder bed, or on a surface that has already been scanned by the laser. Due to the larger size of aforementioned particles compared to fresh powder, this locally increases the layer thickness. The layer thickness is an essential element in an effective building process. An increase in layer thickness may prevent the laser beam from fully melting the current layer and fusing it to the previous layer. This may give rise to pores and lack of fusion in the SLM-manufactured part [27]. Particle redeposition may also occur on parts of the powder bed that have already been scanned. In this case, the redeposited particles may disturb the uniform distribution of the next powder layer(s) by the recoater. Again, this may locally increase the powder layer and give rise to LOF defects. Gong et al. [28] reported defects (pits) caused by the recoater removing large redeposited particles. This is visualized in Figure 7.
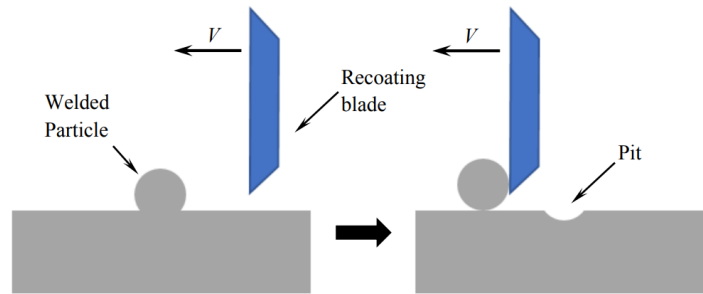
Figure 7: Example of damage sustained through recoater removal of redeposited spatter, as described in Gong et al. [28].

The previous sections described the formation of process by-products and their influence on the SLM process. Insufficient gas flow rate over the build plate may lead to inadequate removal of process by-products, which may lead to defects or lack of fusion in the final part. Ferrar et al. [11] investigated the influence of inert gas flow on porosity and mechanical properties of SLM-manufactured parts. Their findings were that the nonuniform flow over the build plate could be directly linked to the inhomogeneity of the part porosity, as is shown in Figure 8.
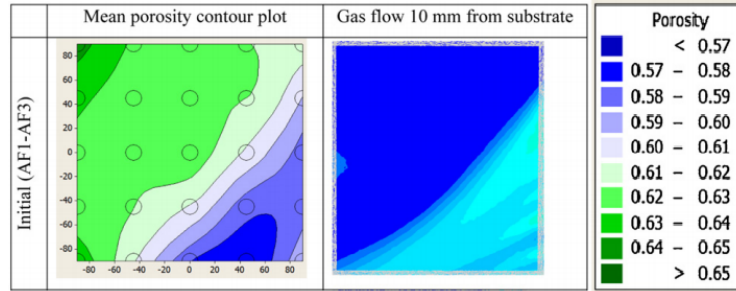
Figure 8: Porosity distribution in test samples and gas flow over substrate [11]

2.2.3 Convective cooling of laser melt pool

The third influence of the inert gas on the SLM process is through convective cooling of the laser melt pool. Figure 9 shows a schematic of heat transfer paths in melt pool formation and solidification in the SLM process. One of the heat transfer paths is through convective heat flow. The amount of heat transferred away from the melt pool through convection is a function of the type of inert gas, as well as gas flow velocity [16]. Since melt pool temperature is a delicate aspect of the SLM process, varying gas flow velocity may lead to over- or under-melting. Both may give rise to melt pool instabilities, negatively affecting the properties of the printed parts.

Figure 9: Heat transfer paths in melt pool formation and solidification in a selective laser melting (SLM) process. [16]

If the melt pool temperature is too high (over-melting), strong dynamical melt flow may generate pore defects, material spattering and denudation zones. Khairallah et al. [29] modelled melt pool physics and found that strong temperature gradients

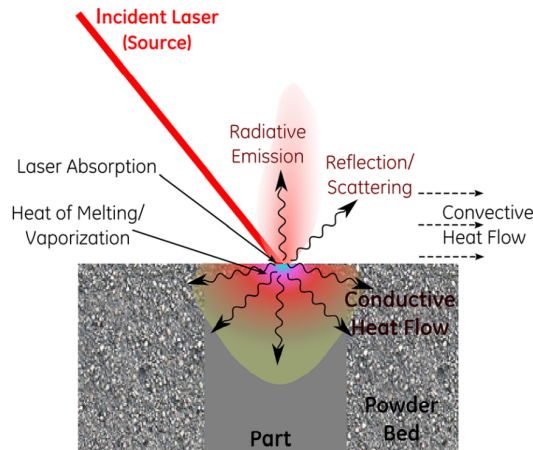below the laser necessitated enabling temperature dependent surface tension, which created Marangoni effects. The Marangoni effect is a mass transfer phenomenon in which fluid from areas with low surface tension is transferred to areas with high surface tension. Previous research indicated that the melt pool fluid flow in SLM is dominated by the Marangoni convection effect caused by the surface tension gradient [30]. Marangoni effects in the melt pool increase melt depth, recirculate the melt flow and lead to spatter ejection from the melt pool [29].

An increase in gas flow velocity leads to an increase in heat transferred through convection, cooling both the melt pool and the rest of the powder bed. This may lead to: 1) Lower temperatures in the melt pool through lower powder bed temperature, 2) Higher thermal gradients around the melt pool through more rapid cooling and solidification of the laser melt pool. As explained earlier, temperature in the melt pool should be high enough to fuse the current molten layer to the previous layer, otherwise LOF pores may arise in the final microstructure due to under-melting. Furthermore, lower temperatures in the laser melt pool may lead to a thinner melt track, which allows humping irregularities to form in the printed parts through the Plateau Rayleigh or Rayleigh-Taylor capillary instability [31]. Thermal gradients created in SLM drive the creation of high residual stresses in the manufactured part [32]. During the SLM process, steep thermal gradients around the melt pool result in inhomogeneous shrinkage during fast cooling, inevitably triggering high residual stresses [33, 34]. Higher convective cooling through inert gas flow steepens the thermal gradients, therefore increasing the residual stresses in the final part. Residual stresses may trigger cracking, delamination and fatigue-failure in 3D-printed components [35].

2.3   System description and scope

As was found by Ferrar et al. [11], nonuniform flow over the powder bed may lead to nonuniform material properties. Therefore, it is necessary to first establish a thorough understanding of the inert gas flow behavior, before a comprehensive evaluation of inert gas flow influence on material properties could be conducted. Therefore, this project consisted of two distinct stages: 1) Gaining a thorough understanding of the gas flow behavior in the build chamber, 2) Evaluation of gas flow influence on material properties.
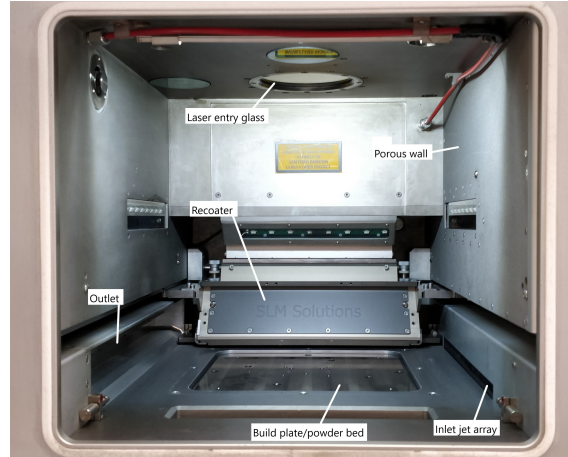
Figure 10: SLM 280HL build chamber with relevant parts annotated.

Figure 10 shows the build chamber of the SLM 280HL. Figure 11 contains a system description of the SLM 280HL system. Three main inputs to the SLM process were defined: a CAD file of the part to be printed, a set of process parameters (Section 4.1), and materials (material powder, inert gas). In this project, a distinction was made between gas-related process parameters and non-gas-related process parameters. The CAD file of the part is sliced into layers according to the predefined layer thickness. Prior to the part production, an inert atmosphere is created in the SLM 280HL build chamber. The build chamber is purged with argon gas, until predefined process conditions are achieved. Then, the iterative manufacturing process starts, which consists of three steps: 1) The build platform is lowered with the predefined layer thickness, 2) A fresh powder layer is deposited on top of the previous layer by the recoater, 3) The laser selectively melts areas of the fresh powder bed according to the sliced CAD file. This three-step process is repeated for every slice of the CAD file. After completion of all slices, the build process has finished and the printed parts can be removed. In the project, printed test specimens did not undergo post-treatment to improve material properties (such as heat treatment to improve microstructure), to get unbiased experimental results. However, post-treatment in the form of sample preparation was required for some experimental tests.
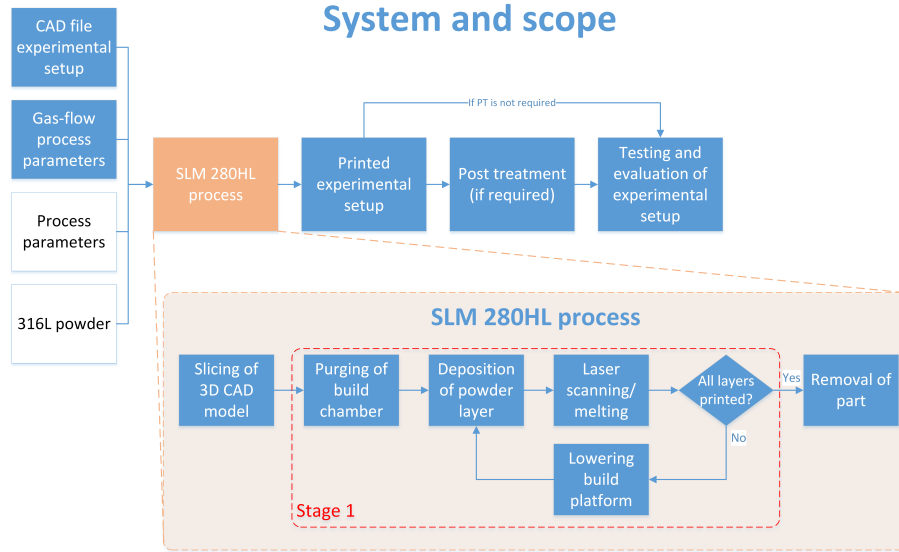
Figure 11: System description of the SLM 280HL process. Emphasized in the blue boxes are the process steps which were included in the scope of the project. The white boxes were outside the scope of this study. Emphasized in the red dotted box is the focus of Stage 1 of the project.

In Section 2.2, three influences of the inert gas flow were explored. The first influence, creation of an inert atmosphere, was outside of the scope of this project. In the experiments conducted in this project, no deviations from the default atmosphere composition were made (argon, <0.1 % O_2). This study was mainly focused on the effects of varying gas flow velocities, which is concerned with the other two influences of the inert gas flow: transport of process by-products and convective cooling of the laser melt pool.

Due to the limited MDP timeframe of 4.5 months, setting a clear scope was a key requirement for a successful project. Forming a thorough understanding of gas flow dynamics and uniformity in the SLM 280HL build chamber was included in this scope. In the remaining time of the project, the relation between gas flow and printing quality was evaluated. Initially, the following quality metrics were included in the project's scope: surface roughness, microstructure and internal residual stresses. These were chosen in consultation with the project's stakeholders. Unfortunately, the evaluation of internal residual stresses was eventually excluded from the project's scope due to setbacks regarding the SLM 280HL's availability (see Section 7). Literature relating inert gas flow to surface roughness was found to be very limited, therefore, this choice of metric also added to the existing knowledge base.

2.4   Problem statement

After in-depth analysis of the research problem, the following problem statement was formulated:

- *The ICD-AM group has limited knowledge of the behavior and uniformity of inert gas flow during the SLM process, and the influence of the inert gas flow on the printing quality of the SLM 280HL.*

3 Research outline

In this section, the research outline for this MDP is provided. The research outline includes the SMART research objective and research (sub)questions. Furthermore, available methods and tools are explored. Finally, the design artifacts and validation processes are stated.

3.1 Research goal

A research objective was formulated according to the SMART-acronym [36]:

- *To provide the ICD-AM group with a thorough understanding of the uniformity and behavior of the inert gas flow during the SLM 280HL process and its influence on surface roughness and microstructure of the printed parts. This is achieved through simulations, measurements and experiments, within the specified timeframe for the MDP.*

3.2 Research questions

A strong research question, well-connected to the research problem, goal and scope, was necessary to guide the project.

- *How does the inert gas flow in the SLM 280HL behave and what is its influence on printing quality?*

This main research question was split up into manageable sub-questions:

- *How does the inert gas flow behave in the SLM 280HL build chamber, and is it uniform across the build plate?*

- *What is the influence of the inert gas flow on printing quality of the SLM 280HL? Is there a statistical correlation between gas flow velocity and material properties?*

3.3 Methods and tools

In this section, available methods and tools to answer the research (sub)question(s) are explored. Methods and tools originate from a literature research, as well as consultation with the problem owner and stakeholders.

3.3.1 Measurement and visualization of inert gas flow behavior in the build chamber

Connected to the first research subquestion, the first stage of the project focused on gas flow dynamics in the build chamber. To analyze the flow, gas flow measurements in the build chamber were conducted using hot-wire anemometry (HWA). Previous studies, such as Philo et al. [37] and Schniedenharn et al. [38], have equipped HWA in similar applications. HWA measures the flow rate through the cooling effects of the gas stream on the hot-wire, which is heated by electrical current [39]. In this project, a PCE-423 hot-wire anemometer by PCE Instruments was used. CFD simulations in COMSOL Multiphysics 5.6 were used as an additional tool to gain an understanding of the gas flow in the SLM 280HL's build chamber, as was also done by Ferrar et al. [11], Philo et al. [37] and Chen et al. [40]. Results of the HWA measurements were used as an input for the CFD model (inlet flow velocities).

3.3.2 Evaluation of inert gas flow influence on printing quality metrics

As mentioned in Section 2.3, surface roughness and microstructure were evaluated in this project. Porosity was also analyzed during the microstructure analysis.

Evaluation methods of the material properties were chosen based on the available methods at Philips, NTS-Norma, Stork and the University of Groningen. The surface roughness measurements were conducted using a contact stylus profilometer (a MarSurf PS10 by Mahr), which measured the surface roughness (R_a and R_z) over a predefined segment length. The microstructure of the samples was studied using an optical microscope, similarly to Nguyen et al. [12]. Porosity analysis was conducted using optical microscopy images of sample cross-sections. Microscopy images were binarized in ImageJ and subsequently analyzed in MATLAB.

To determine the statistical significance of the experimental results, the data was analyzed using Minitab statistical software. Various statistical models were employed: a two-sample t-test (also known as an independent samples t-test), a one-way Analysis of Variance (ANOVA) and a fit regression model. ANOVA was also used in Ferrar et al. [11] and Anwar & Pham [13].

3.4 Design artifact and validation

Two design artifacts were delivered and validated in this MDP. The first design artifact was a COMSOL CFD model, which provides a numerical solution for the inert gas flow inside the SLM 280HL build chamber. Validation of the COMSOL model was conducted with the measured flow velocity data. Whereas the measured flow velocity data (near the inlets) also served as an input for the COMSOL model,

measured values in other areas of the build chamber (over the build plate) could be used for the validation of the COMSOL model. The measured data points (actual values) were compared to data points in the COMSOL solution (simulated values). The mean absolute percentage error (M) was computed at each data point.

$$M = 100\% \frac{\sum\limits_{t=1}^{n} \left| \frac{A_t - F_t}{A_t} \right|}{n} \qquad (1)$$

where A_t is the measured value at a data point, F_t is the simulated value at a data point, and n is the number of values.

The design of experiments to evaluate material properties was regarded as the second design artifact in this MDP. Batches of experimental samples were SLM-manufactured and evaluated through experiments. The design of the experimental batches and the experimental approach to evaluate the material properties strongly determined the quality and value of the experimental results. The results of the experiments were validated with statistical tools (Section 3.3.2).

4 Materials and methods

In this section, the design of experiments is presented.

4.1 SLM 280HL

The process parameters for the SLM-manufactured experimental batches are shown in Table 1.

Table 1: SLM 280HL build parameters for the experimental batches.

Build parameters	Value
Border - Laser power	100 W
Border - Scan speed	600 mm/s
Hatch - Laser power	190 W
Hatch - Scan speed	750 mm/s
Hatch spacing	0.12 mm
Layer thickness	0.03 mm
Scanning strategy	Stripes
Argon flow velocity	12 & 18 m/s

The SLM 280HL is equipped with an argon flow sensor, which is located within the feedback piping of the machine (Figure 12). Based on the input of this flow sensor, the SLM 280HL controls the gas flow velocity at a predefined input parameter. The default parameter value used within the ICD-AM group is 18 m/s. Included in the scope of the measurements and experiments were the default velocity setting (18 m/s) and a significantly lower velocity setting (12 m/s). Due to the timeframe of the project, it was not feasible to evaluate a wider range of flow velocities.

The material powder chosen for the experimental print batches in this project is 316L stainless steel. The SLM research within the ICD-AM group is currently most focused on 316L. Since changing material powder in the SLM 280HL is time-consuming, it was most convenient to use 316L material powder for the experimental batches in this project.

4.2 Experiment I: Visualization of inert gas flow behavior in build chamber

As emphasized throughout the report, the first step in the experimental phase of the project was focused on gaining a thorough understanding of inert gas flow behavior

throughout the build chamber. Hot-wire anemometry and CFD simulations were chosen as the appropriate tools to achieve this goal.

4.2.1 Calibration of hot-wire anemometer

The hot-wire anemometer used in this project, a PCE-423, returns a measured flow velocity and temperature to the operator. However, the anemometer was calibrated for air instead of argon. Convective heat transfer coefficient and thermal conductivity are gas properties which directly influence the output of the hot-wire anemometer. Since these properties are different for air and argon, calibration of the PCE-423 for argon measurements was necessary.
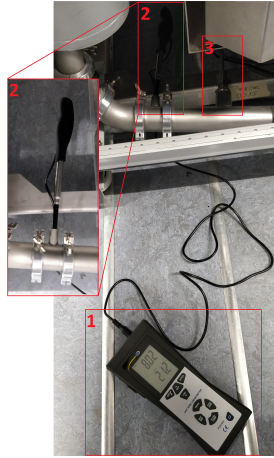

Figure 12: Experimental setup for PCE-423 argon calibration. 1) PCE-423, 2) PCE-423 measurement probe, 3) SLM 280HL built-in argon flow velocity sensor.

The SLM 280HL features a built-in argon flow velocity sensor, located in the feedback piping of the machine. By placing the PCE-423 measuring probe inside the feedback piping near the SLM 280HL velocity sensor, a relation between the measured PCE-423 air velocity and the actual argon velocity could be derived. The calibration setup is shown in Figure 12. The flow velocity setting on the SLM 280HL was swept from 6-23 m/s, with a step size of 1 m/s. In thermal anemometry, the gas temperature is also a parameter influencing the measurements. Therefore, the calibration experiment was conducted at two different gas temperatures (24.15 °C and 29.45 °C). The gas temperature was regulated using build plate heating in the build chamber.

4.2.2 Gas flow measurements in the build chamber

After calibration, the PCE-423 was deployed for flow measurements inside the build chamber. To get representative measurement data, near-process conditions were created in the build chamber. The PCE-423, which does not require a power cable, could be placed inside the sealed build chamber during the experiments and was operated using the rubber glove in the build chamber door (Figure 13). Therefore, an inert atmosphere with low oxygen levels (<0.5%) could be created in the build chamber. Measurements were conducted at two SLM 280HL flow velocity settings: 12 m/s and 18 m/s. The measurement conditions are noted in Table 2.
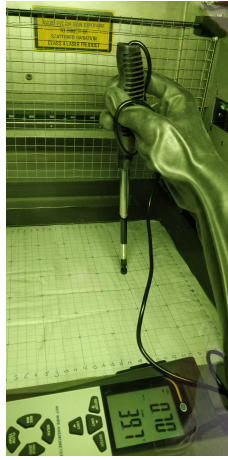

Figure 13: Flow measurements over the build plate being conducted. The rubber glove provides access to operate the PCE-423.

Table 2: Build chamber measurement conditions

Process parameter	Value
Inert gas type	Argon
Oxygen %	< 0.5 %
Build chamber temperature range	between 30.4 and 40.2 °C
Argon flow velocity (SLM 280HL setting)	12 m/s & 18 m/s
Overpressure in system	12 mbar

At near-process conditions, flow velocity measurements were conducted at several areas in the build chamber (see Figure 10):

- In front of each of the 70 jets in the lower inlet jet array.

- In front of the porous wall.

- Over the build plate. The flow was measured at 145 locations, according to a 29x5 grid, which is shown in Figure 14. The PCE-423 hot-wire (which measures the flow velocity) measured the flow velocity 9 mm above the build plate.

The measurements in front of the inlet jet array and the porous wall served as inputs to the CFD model. The measurements over the build plate were used to validate the CFD model.
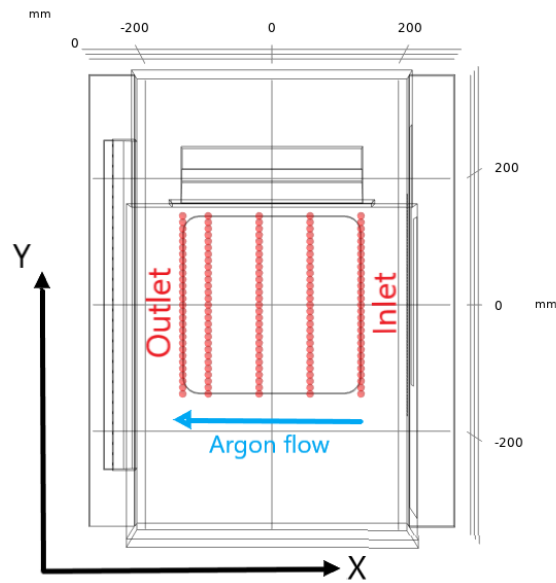

Figure 14: Top view of SLM 280HL build chamber, with locations of build plate flow velocity measurements. Each red dot corresponds to a measurement location.

4.2.3 COMSOL CFD simulations

A CFD study was conducted to visualize the build chamber flow and to simulate varying scenarios. The SLM 280HL's build chamber was replicated in COMSOL using measured dimensions. Argon (properties in Table 3) was fed into the build chamber through the inlet jet array and the porous wall according to the data from the flow measurement experiment. Flow dynamics were modelled using the k-ϵ turbulence model, just like in Chen et al. [40] and Wang et al. [41]. A physics-controlled mesh was chosen, which was refined between the inlet array and the outlet (shown in Figure 15). Evaluation of the build plate flow profile was the main scope of Stage 1 of the project, and therefore, the solution should be most accurate here. Furthermore, flow velocities are much higher close to the build plate compared to the

rest of the build chamber. Therefore, mesh refinement was chosen in this domain.

Table 3: Argon properties used in COMSOL, corrected for temperature and pressure. 31.03 °C and 36.05 °C are the average temperatures at which the 12 m/s and 18 m/s measurements were conducted, respectively.

Argon property	Value
Density (31.03°C)	1.6218 $\frac{kg}{m^3}$
Dynamic viscosity (31.03°C)	2.2999*10^{-5} Pa*s
Density (36.05°C)	1.5958 $\frac{kg}{m^3}$
Dynamic viscosity (36.05°C)	2.3316*10^{-5} Pa*s
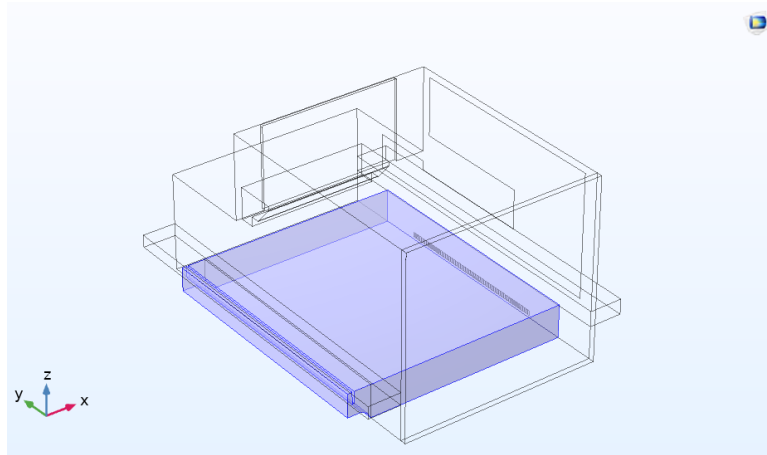
Figure 15: Domain of COMSOL geometry in which mesh refinement was applied.

As mentioned earlier, the COMSOL model was validated using a MAPE-comparison to the measured data. Appendix A provides the geometry, materials, physics and mesh of the COMSOL CFD model.

4.3 Experiment II: Evaluation of inert gas flow influence on surface roughness and microstructure

After a thorough understanding of the gas flow dynamics in the build chamber was formed, the influence of the argon gas flow on surface roughness and microstructure was investigated.

4.3.1 Sample and batch design

To save time and material, the experimental print batches for surface roughness and microstructure evaluation were combined. Surface roughness was measured using a non-destructive technique (Section 4.3.2), and therefore, the samples could be used for microstructure analysis after surface roughness data was gathered.
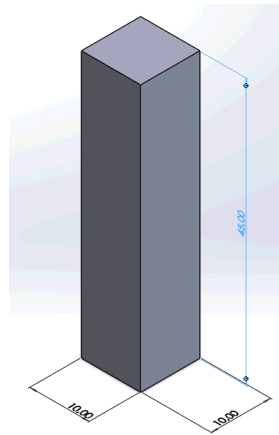

Figure 16: Sample design for surface roughness and microstructure analysis. Dimensions are in mm.

The sample design satisfied a number of requirements. A flat surface of sufficient size was required for surface roughness measurements. Furthermore, a cross-section suitable for microstructure analysis had to be produced from the sample. This ruled out the possibility of a shell-design to save material. The sample design is shown in Figure 16. It featured two surfaces of 10x45 mm parallel to the flow direction, which were produced under similar circumstances. Therefore, surface roughness measurements could be performed on two independent, yet similar surfaces for each sample. This doubled the sample size, and therefore, the statistical significance of the results.
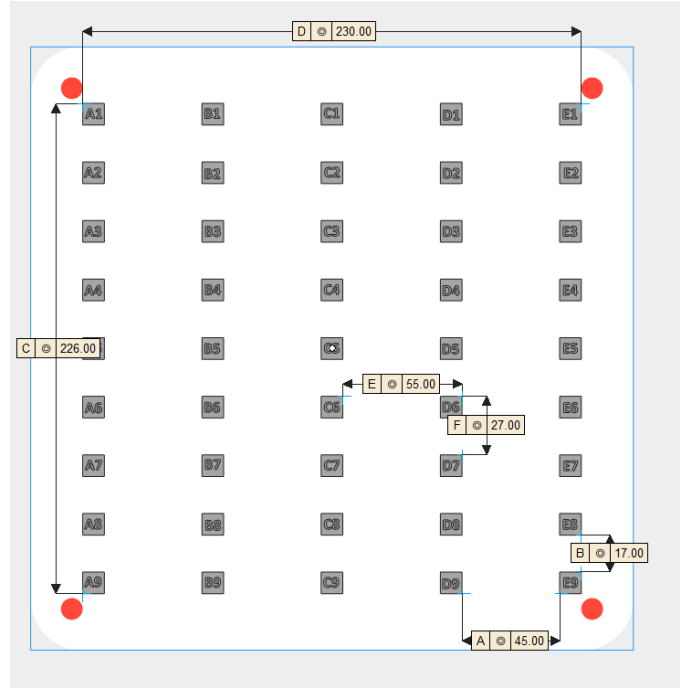
Figure 17: Top view of batch layout for surface roughness and microstructure analysis. The red circles indicate screw holes for the build plate. Annotated distances are in mm.

In Figure 17, a top view of the batch design for the surface roughness and microstructure analysis is shown. Each square refers to a sample shown in Figure 16. Each sample was printed on top of 5 mm of support structures. The samples were spread out over the surface of the build plate. Therefore, variation in material properties within a build (intra-build variation) could be evaluated. The flow profile over the build plate may be linked to the (non)uniformity of material properties over the build plate, as in Ferrar et al. [11].

As mentioned in Section 4.1, two batches were fabricated: at 12 m/s and 18 m/s. Apart from gas flow velocity, all process parameters and building conditions were similar for both batches.

4.3.2 Evaluation method of surface roughness

The surface roughness was measured using a Mahr MarSurf PS10 contact profilometer, which utilizes a diamond stylus to measure the profile of the surface. Two surface roughness parameters were calculated: R_a and R_z. R_a measures the average length between the peaks and valleys and the deviation from the mean line over the mea-

sured segment. R_z measures the vertical distance between the highest peak to the lowest valley over five sampling lengths and averages the values [42]. Both R_a and R_z are expressed in μm throughout this report. Three 12.5 mm segments (high, middle and low) were measured on each of the sample's surfaces parallel to the flow, for a total of six measurements per sample. For each segment, the contact profilometer returned R_a and R_z. R_z was evaluated over five 2.5 mm sampling lengths.

4.3.3 Evaluation method of microstructure

Microstructure analysis was performed on a cross-section of the samples, which is shown in Figure 18. Therefore, all surface roughness data had to be gathered before the samples could be cut for the microstructure analysis.
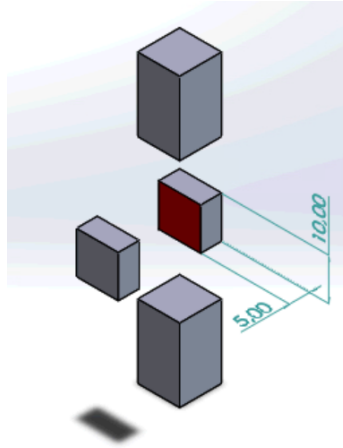

Figure 18: Sample design for surface roughness and microstructure analysis. The boundary shown in red was examined under an optical microscope. Dimensions are in mm.

The cross-sections of the samples were polished and etched, after which they were examined under an optical microscope (2.5x-100x magnification). The microstructure analysis was too time consuming to perform for all samples, therefore, a total of six samples from each batch (12 m/s and 18 m/s) were selected for microstructural analysis. Samples A2, A5 and A8 were compared to samples E2, E5 and E8 (see Figure 17). These samples were chosen since column A and E are located furthest from and closest to the inlet, respectively. The argon flowing over column E has a higher velocity than the argon flowing over column A. Therefore, transport of process by-products and prevention of beam attenuation might be more effective in column E. Furthermore, the argon flowing over column A is contaminated with process by-products from four preceding columns printed upstream. Therefore, it was

expected that this choice of samples yielded the best results in the microstructure analysis, especially concerning possible effects of redeposition in the microstructure. The goal of this analysis was to investigate the microstructure of the samples produced at 12 m/s and 18 m/s, as well as to evaluate the effects of build plate position on microstructure. Based off the literature review, it was hypothesized that the microstructure of the samples produced at 12 m/s would show lower fusion between layers and higher porosity compared to the samples produced at 18 m/s, due to less effective transport of process by-products.

5 Results and discussion

In this section, the results of the measurements, simulations and experiments are presented. First, the results of the flow measurements and simulations are presented. These results were used in the interpretation of the subsequent experiments.

5.1 Results of Experiment I: Visualization of inert gas flow behavior in build chamber

5.1.1 Calibration

Argon calibration of the PCE-423 is conducted at two gas temperatures: 24.15 °C and 29.45 °C. The results of the calibration are shown in Figure 19. A linear trendline was fitted through the data points and the origin. The R-squared statistic confirms a good linear fit of the calibration data at both temperatures.
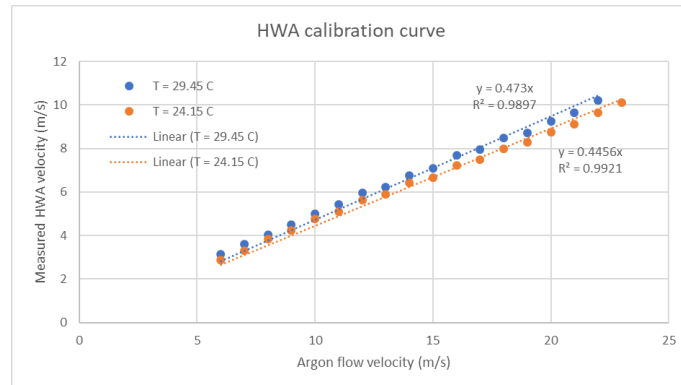

Figure 19: Data points of HWA calibration fitted with linear trendline. Measurements were conducted at 24.15 °C (orange graph) and at 29.45 °C (blue graph).

As mentioned in Section 4.2.1, the gas temperature was expected to influence the measurements and the calibration data. The two linear calibration graphs shown in Figure 19 display different slopes, therefore confirming the influence of gas temperature on the measured data. Under the assumption that the slope of the calibration graph is linearly dependent on the temperature, a calibration coefficient for the measured HWA velocity could be derived for any temperature using the two graphs in Figure 19. Analytical calculations using the equations underlying hot-wire anemometry justified this assumption.

5.1.2 Measurements

Flow measurements in the build chamber were conducted using the PCE-423 and the calibration data. Three series of measurements in front of the inlet jet array were conducted, of which the results are shown in Figure 20. The flow profile in front of the inlet jet array was found to be nonuniform. The wave-shaped flow profile was significantly lower in the middle of the array than towards the sides. The measured argon flow velocity profile in front of the porous wall was 0.2 m/s at 12 m/s and 0.3 m/s at 18 m/s.
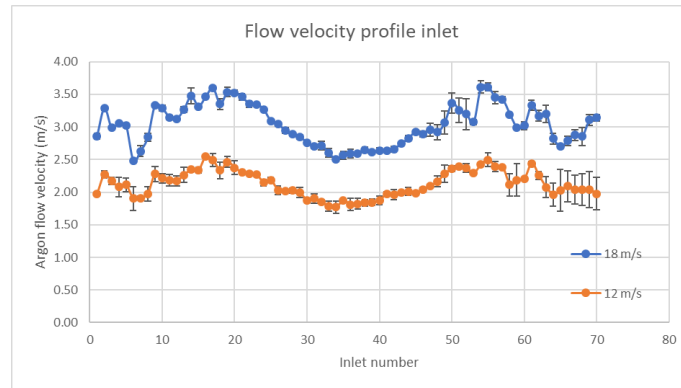
Figure 20: Temperature-corrected measured flow velocities in front of the inlet jet array, for a SLM 280HL velocity setting of 12 m/s (orange graph) and 18 m/s (blue graph). The X-axis shows the inlet jet number corresponding to each data point. Inlet 1 is located closest to the build chamber door, inlet 70 is located closest to the rear wall of the build chamber. The total inlet array consists of 70 inlet jets.

The results of the flow measurements over the build plate at 12 m/s and 18 m/s are shown in Figures 21 and 22. The build plate flow profile displayed similar nonuniform characteristics as the inlet jet array. Since the inlet jet array feeds in the argon flowing over the build plate, this was expected beforehand.

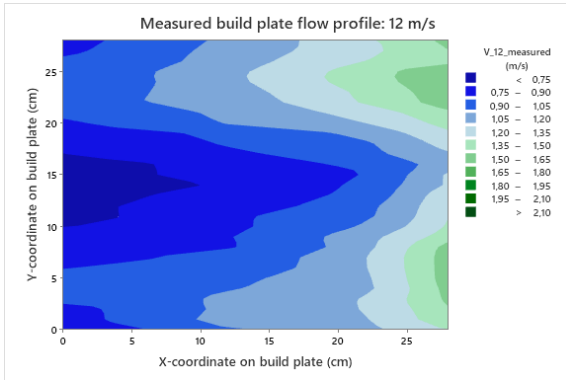Figure 21: Flow profile 9 mm above build plate for 12 m/s SLM 280HL flow velocity setting.
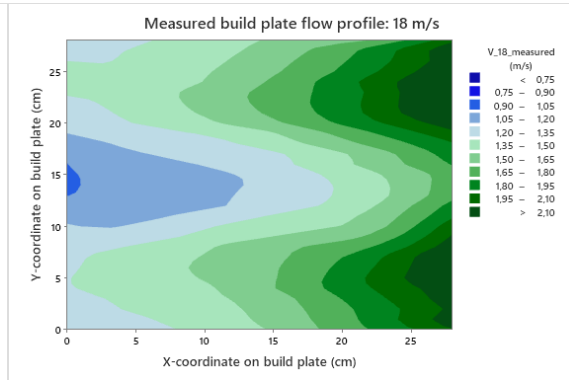
Figure 22: Flow profile 9 mm above build plate for 18 m/s SLM 280HL flow velocity setting.

5.1.3 CFD simulations

The COMSOL flow profile computed 9 mm above the build plate is shown in Figures 23 and 24. This height is comparable to the height at which the flow measurements over the build plate were conducted.
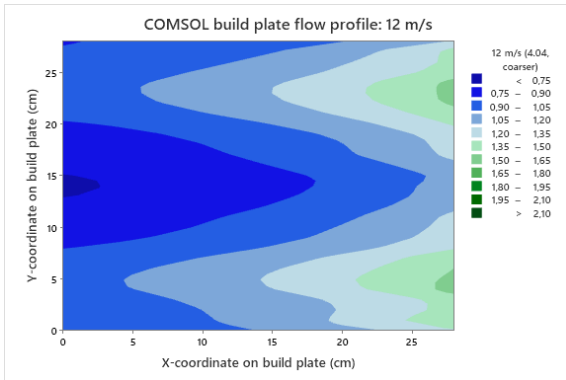
Figure 23: Contour plot of COM-SOL build plate flow profile at 12 m/s. Mesh size: 4.04, coarser (Appendix A).
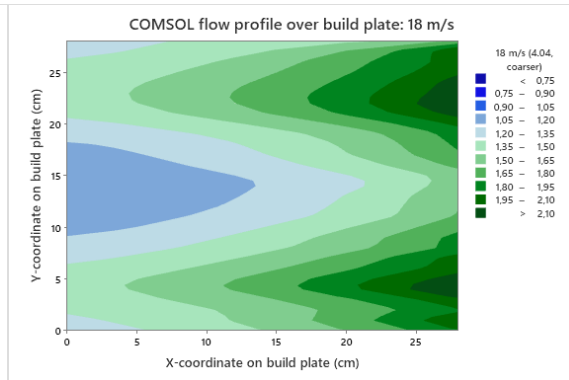
Figure 24: Contour plot of COM-SOL build plate flow profile at 18 m/s. Mesh size: 4.04, coarser (Appendix A).

A comparison between the measured and computed flow profiles was conducted to validate the CFD model. The MAPE, explained in Section 3.4, was computed to express the difference between the flow profiles. At the finest mesh setting, the 12 m/s measured flow profile was approached with a MAPE of 6.19%. At 18 m/s, the MAPE was 4.60%. These errors were deemed low enough to utilize the COMSOL

model for the visualization of build chamber flow dynamics, and to simulate varying scenarios. Figure 25 shows the MAPE for several mesh sizes. It can be seen that increasing the complexity of the mesh yielded a more accurate solution, which would be expected. The low MAPE values and the theoretically expected behavior of the MAPE for increasing mesh complexity validated the COMSOL model.
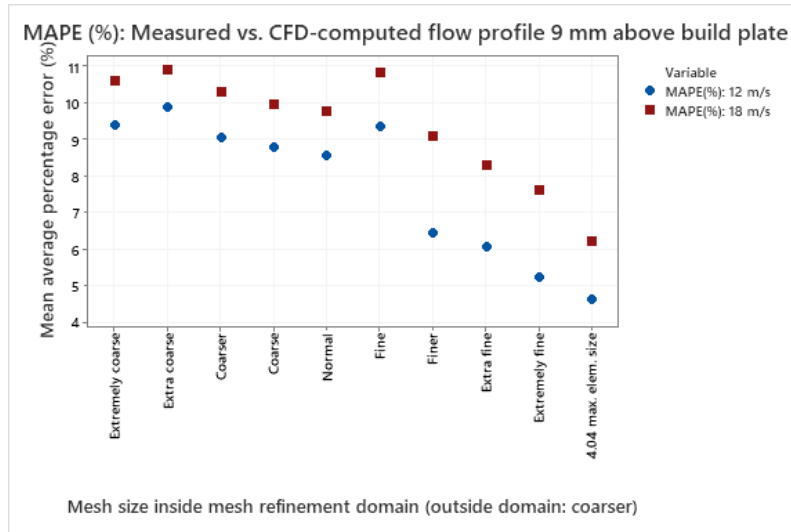
Figure 25: MAPE of COMSOL flow profile compared to measured data. The X-axis shows the mesh size inside the mesh refinement domain (Figure 15). Details of the mesh refinement study can be found in Appendix A.

Figure 26 shows a streamline plot of the flow in the build chamber at 18 m/s. Figures 27 and 28 show a side view of the argon flow in the build chamber for 12 m/s and 18 m/s. It can be seen that most of the argon fed into the build chamber flowed directly to the outlet.
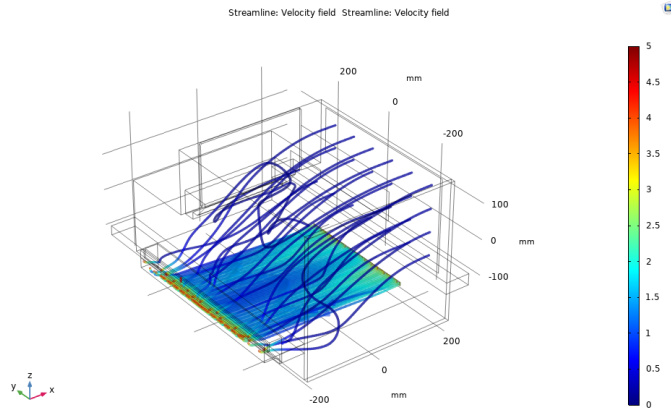
Figure 26: Streamline plot in COMSOL. Mesh size: 4.04, coarser (Appendix A).
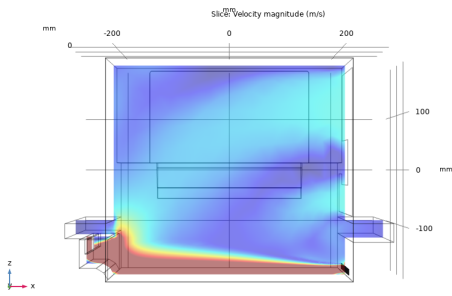
Figure 27: Side-view of build chamber flow profile in COMSOL at 12 m/s. Mesh size: 4.04, coarser.
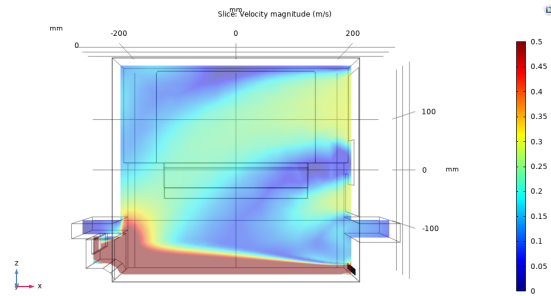
Figure 28: Side-view of build chamber flow profile in COMSOL at 18 m/s. Mesh size: 4.04, coarser.

In the past, engineers within ICD-AM observed that the pores in the porous wall would gradually become blocked with process by-products, leading to reduced permeability. Therefore, less argon entered the build chamber through the porous wall. Another phenomenon observed by the engineers was that the laser entry glass (Figure 10) would get contaminated with metal spatter and process by-products over time. It was hypothesized that the reduced flow rate through the porous wall led to inadequate removal of process by-products, and therefore, to the observed contamination of the laser glass. The COMSOL model was deployed to test this hypothesis. Figures 29 and 30 show the side view streamline plots of the argon flow velocity in the build chamber for two situations: 1) A porous wall flow rate of 0.3 m/s at 18 m/s (clean, unblocked porous wall) and, 2) A porous wall flow rate of 0.2 m/s at 18 m/s (simulating a blocked porous wall). It can be seen that for situation 1

(Figure 29), most of the argon flowed directly to the outlet. For situation 2 (Figure 30), much recirculation of the argon in the build chamber volume was visible. A function of the porous wall inflow is to deflect and intercept spatter from the laser melt pool which is ejected towards the laser glass. In situation 2, the effectiveness of the porous wall flow at intercepting ejected spatter might be reduced due to the lower inflow velocity and the nonuniform build chamber behavior. Additionally, some of the flow over the build plate, which may carry process by-products, was recirculated in the build chamber volume instead of flowing directly to the outlet. This may be an additional cause of faster laser glass contamination in situation 2. In conclusion, the CFD simulation supported the hypothesis stated by the ICD-AM engineers: There may be a relation between the observed laser glass contamination and the blockage of the porous wall. However, more in-depth research is needed to confirm the hypothesis.
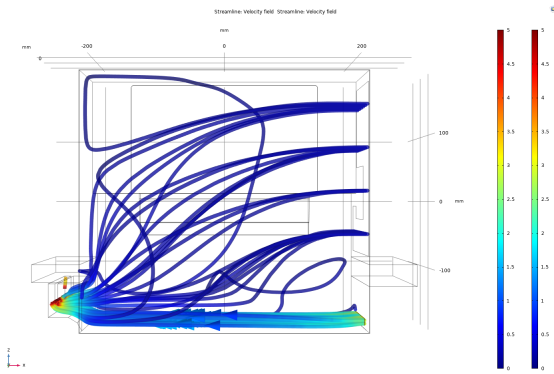
Figure 29: Side view of build chamber containing streamline plot for a porous wall inflow of 0.3 m/s. Mesh size: finer, coarser (Appendix A).
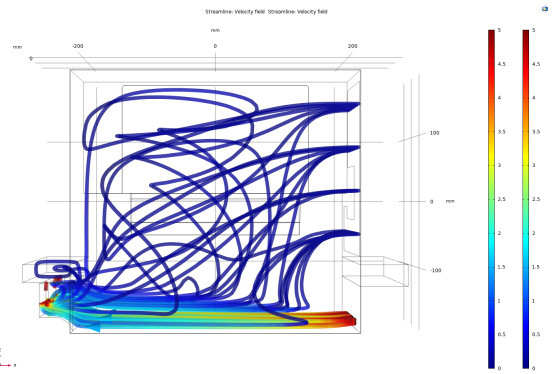
Figure 30: Side view of build chamber containing streamline plot for a porous wall inflow of 0.2 m/s. Mesh size: finer, coarser (Appendix A).

5.2 Results of Experiment II: Evaluation of inert gas flow influence on surface roughness and microstructure

Two experimental batches were printed to evaluate the influence of inert gas flow on surface roughness and microstructure:

- Batch 1: surface roughness and microstructure, 18 m/s.

- Batch 2: surface roughness and microstructure, 12 m/s.

5.2.1 Surface roughness

Inter-build (between two separate batches) variation of surface roughness was evaluated for R_a and R_z. The two data sets were evaluated in Minitab using a two-sample t-test. The null hypothesis for this test stated that there is no statistically significant difference between the means of the two data sets ($H_0 : \mu_1 - \mu_2 = 0$). A confidence interval of 95% was adopted, meaning that the null hypothesis could be rejected when p<0.05. Figures 31 and 32 show the R_a and R_z boxplots of the two data sets. Table 4 contains descriptive statistics of the data sets, and Table 5 contains the results of the two sample t-test. Both the R_a- and the R_z-test produced a p-value of <0.001. Therefore, the null hypothesis was rejected and the alternative hypothesis ($H_1 : \mu_1 - \mu_2 \neq 0$) was accepted.
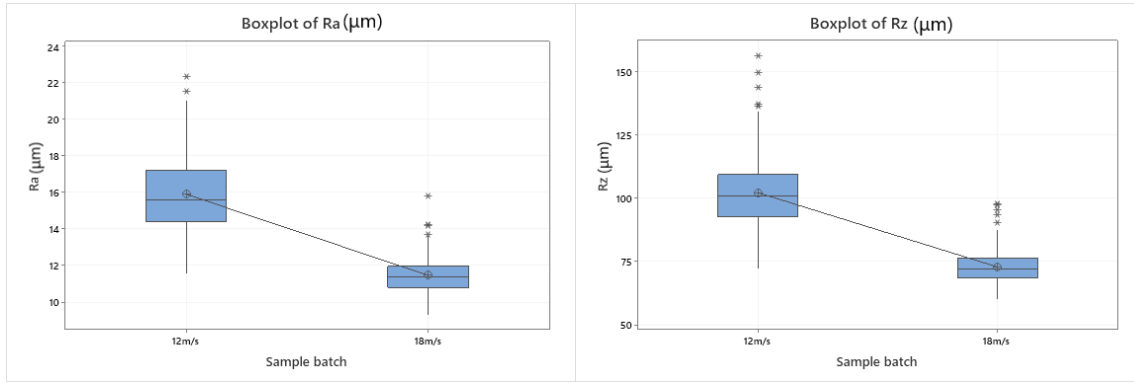
Figure 31: Comparison of Ra data sets, batch printed at 12 m/s versus batch printed at 18 m/s. The sample size of both boxplots is 270 measurements (45 samples, six measurements per sample).

Figure 32: Comparison of Rz data sets, batch printed at 12 m/s versus batch printed at 18 m/s. The sample size of both boxplots is 270 measurements (45 samples, six measurements per sample).

Data set	Sample size	Mean (μm)	StDev (μm)
Ra: 12 m/s	270	15.900	2.010
Ra: 18 m/s	270	11.461	0.938
Rz: 12 m/s	270	102.200	14.100
Rz: 18 m/s	270	72.860	6.870

Table 4: Descriptive statistics of surface roughness data sets printed at 12 m/s and 18 m/s.

Test	T-value	DOF	P-value	Null hypothesis
Ra: 12 m/s vs. 18 m/s	32.87	380	< 0.001	Rejected
Rz: 12 m/s vs. 18 m/s	30.78	390	< 0.001	Rejected

Table 5: Two sample t-test comparing means of Ra and Rz data sets of batches printed at 12 m/s and 18 m/s.

Furthermore, intra-build variation was evaluated. For upstream samples (closer to the inlet), both beam attenuation and redeposition were expected to be less common than for downstream samples. Since both mechanisms introduce irregularities, pores and defects in the samples, surface roughness was expected to be higher on downstream samples. Figure 33 shows the surface roughness contour plots for the batches printed at 12 m/s and 18 m/s. Each data point in the contour plot corresponds to the location of a sample of the build plate (Figure 17). Whereas the velocity profiles at 12 m/s and 18 m/s displayed similar characteristics, the surface roughness profiles were dissimilar. The surface roughness distribution over the build plate for the build at 18 m/s was relatively uniform, both for R_a and R_z. On the other hand, the batch printed at 12 m/s showed significant nonuniformity, both in the R_a- and R_z-profiles. The correlation between flow nonuniformity and surface roughness uniformity over the build plate was tested using a fit regression model in Minitab, taking into account a 95% confidence interval. Regression analysis revealed that for 12 m/s, both R_a and R_z nonuniformity could be linked to the flow profile 9 mm above the build plate. For 18 m/s, a statistically significant correlation was found between the R_z profile and the flow profile 9 mm above the build plate, whereas the correlation between the flow profile and the R_a profile was not deemed statistically significant. The results of the regression analysis and R-values are noted in Tables 6 and 7. An interesting observation in the regression equations and R-values shown in Tables 6 and 7 is that for 12 m/s, the relation between surface roughness and flow velocity is negative, whereas for 18 m/s the relation is positive. In other words, higher flow velocity over the build plate led to lower surface roughness in the 12 m/s build, whereas it led to higher surface roughness in the 18 m/s. A reason for this may be that the surface roughness nonuniformity in the 12 m/s build is mainly caused by mechanisms related to the inadequate transport of process by-products: beam attenuation and redeposition. In the 18 m/s build, transport of process by-products seems to be adequate and the surface roughness nonuniformity may be mainly caused by convective cooling of the laser melt pool by the inert gas flow.
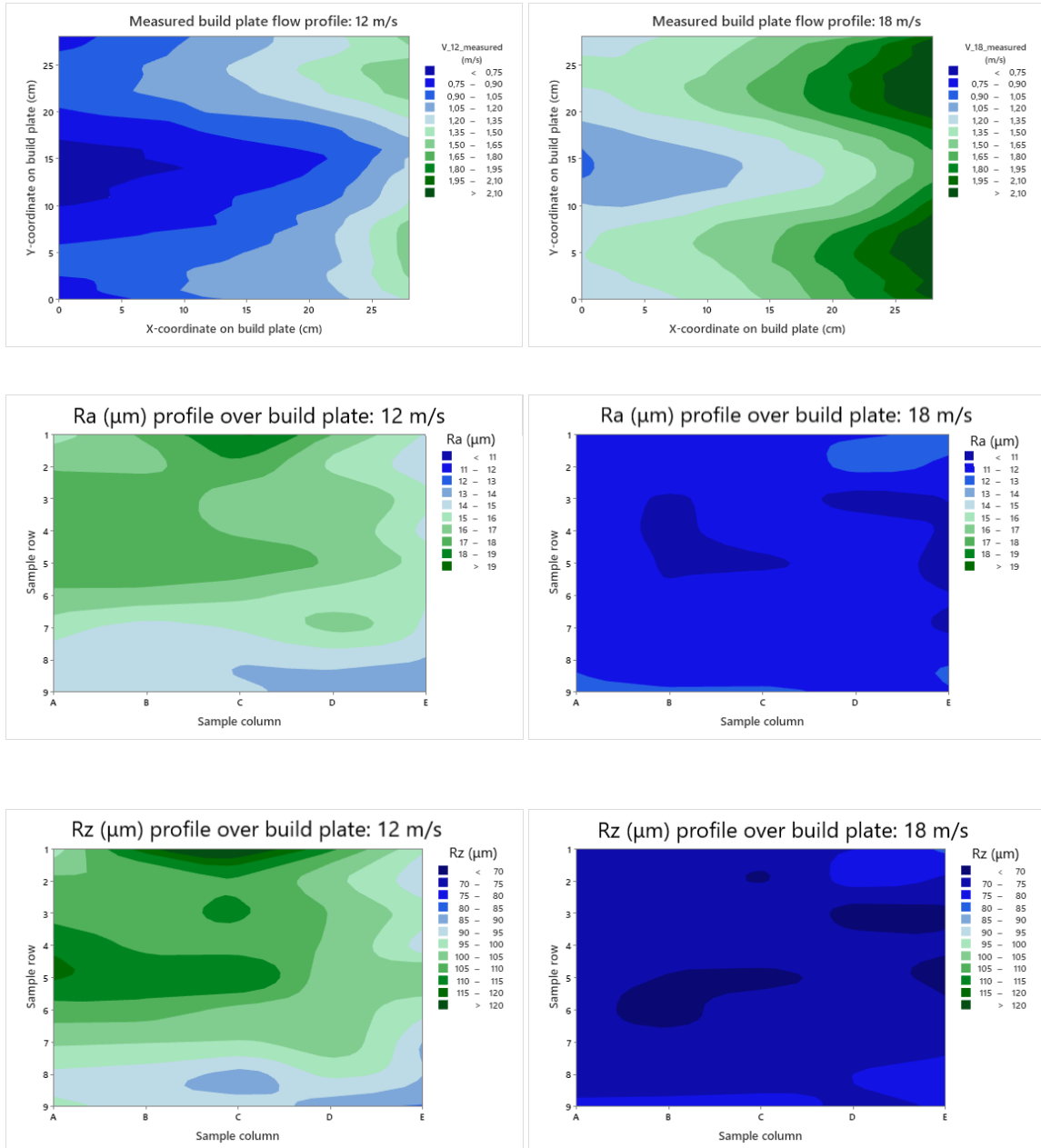
Figure 33: (a)(b) Contour plot of measured flow velocity profile over the build plate (same as Figure 21 and 22 (c)(d) Contour plot of Ra for 12 m/s and 18 m/s (e)(f) Contour plot of Rz for 12 m/s and 18 m/s.

Test	Regression Equation	P-value	Null hypothesis
12 m/s: R_a (μm) vs. V (m/s)	Ra = 12.841 - 2.832V	0.004	Rejected
12 m/s: R_z (μm) vs. V (m/s)	Rz = 121.59 - 18.65V	0.004	Rejected
18 m/s: R_a (μm) vs. V (m/s)	Ra = 10.860 + 0.389V	0.100	Failed to reject
18 m/s: R_z (μm) vs. V (m/s)	Rz = 67.30 + 3.60V	0.021	Rejected

Table 6: Results of regression analysis of surface roughness profile and flow velocity profile over the build plate. The null hypothesis could be rejected for p<0.05.

Test	R-value	Interpretation
12 m/s: R_a (μm) vs. V (m/s)	-0.417	Low negative correlation
12 m/s: R_z (μm) vs. V (m/s)	-0.424	Low negative correlation
18 m/s: R_a (μm) vs. V (m/s)	0.248	Negligible correlation
18 m/s: R_z (μm) vs. V (m/s)	0.344	Low positive correlation

Table 7: R-value analysis of surface roughness profile and flow velocity profile over the build plate.

5.2.2 Microstructure

The polished cross-sections (Figure 18) of the selected samples were examined under an optical microscope. Figures 34 and 35 show the polished microstructures of samples E5 printed at 12 m/s and 18 m/s gas flow velocity. It was obvious that the porosity of the samples printed at 12 m/s was significantly greater than the porosity of the samples printed at 18 m/s. The large size and irregular shape of the pores shown in the microstructure of the 12 m/s samples identified them as LOF pores [43]. LOF pores stem from insufficient penetration of the melt pool into the previous layer [44], which may be a result of reduced laser power (beam attenuation) or locally increased layer thickness of the powder (redeposition). The pores observed in the 18 m/s microstructure were mostly spherical, which indicated that these were either gas pores or keyhole-induced pores. Gas pores are formed through entrapment of gas in the microstructure, which may be atmosphere gas in the melt pool, or gas and moisture present in the powder bed. Lacking sufficient time to escape the melt pool before solidification, the gas bubbles become trapped, forming

pores in the microstructure. Another reason is entrapping gas inside powder particles during the gas atomization process of the powder [45]. However, the irregularly shaped LOF pores are considered as the major defect in the microstructure of SLM-manufactured parts [46]. The pores in the 12 m/s microstructure were mostly LOF pores. Severe lack of fusion between subsequent layers could be observed in the 12 m/s microstructure, an example of which is highlighted in the red box in Figure 34. The effective cross-sectional area of these layers under tensile loading is decreased, therefore increasing the stress in the part. Furthermore, LOF pores may initiate cracks due to high stress concentrations. Liu et al. [15] studied fatigue behavior in SLM-manufactured Ti-6Al-4V specimens, and found that LOF defects were primarily responsible for fatigue crack initiation, therefore leading to reduced fatigue life. Mechanical performance (tensile strength and fatigue life) of the samples printed at 12 m/s is expected to be significantly worse than the samples printed at 18 m/s. This hypothesis was supported by the occurrence of delamination in the 12 m/s samples during the removal of support structures after printing, as is shown in Figures 36 and 37. Delamination indicates the separation of successive print layers due to inappropriate melting overlap with previous underlying solidified powder or incomplete particles melting [47]. The observed delamination in the 12 m/s microstructure indicates poor fusion between successive layers resulting in poor mechanical properties. Analysis of intra-build variance concluded that the samples printed in front of the middle of the inlet jet (samples A5 and E5 at 12 m/s), where flow velocity is lowest, displayed the highest concentration of LOF pores in the microstructure. Lower flow velocity might have led to insufficient removal of process by-products, which might have scattered the laser beam [6]. This introduced insufficient laser power in the melt pool, therefore preventing good fusion between subsequent layers.

The polished microstructure images were used for porosity analysis. The images were binarized in ImageJ, after which the area fraction of pores (porosity) was computed in MATLAB. The entire cross-section of each sample was photographed in six to eight microscopic images. Figures 38 and 39 show the relative density (Equation 2) of the analyzed samples. Each data point in the boxplots corresponds to the relative density of an analyzed image. The descriptive statistics of the data sets are noted in Table 8.

$$\rho_{relative} = 100\% - porosity \tag{2}$$
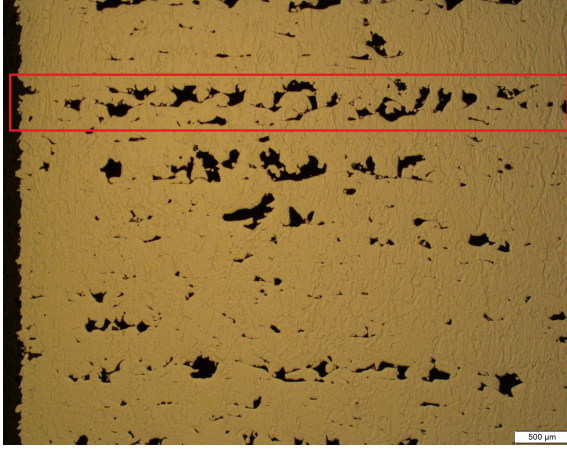
Figure 34: Polished microstructure of sample E5, printed at 12 m/s. The red box highlights an example of severe lack of fusion between layers. Magnification factor is 2.5x.

Figure 35: Polished microstructure of sample E5, printed at 18 m/s. Magnification factor is 2.5x.
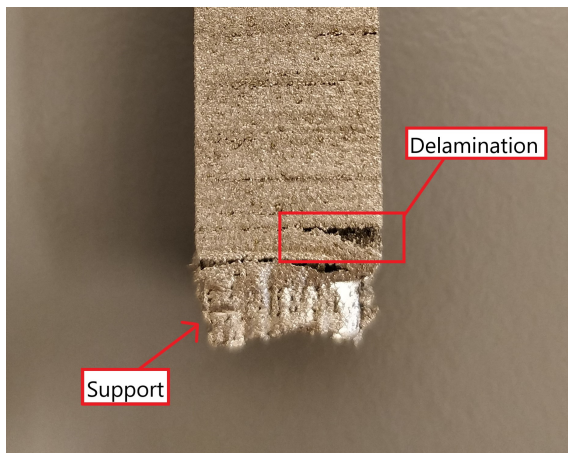
Figure 36: Delamination observed in sample C4, printed at 12 m/s.
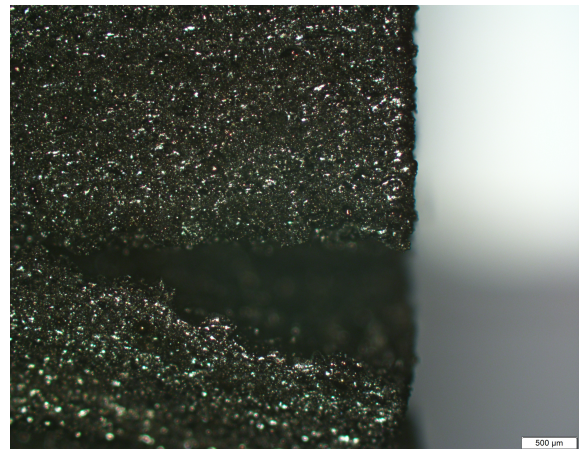
Figure 37: Optical microscopy image of delamination shown in Figure 36. Magnification factor is 2.5x.
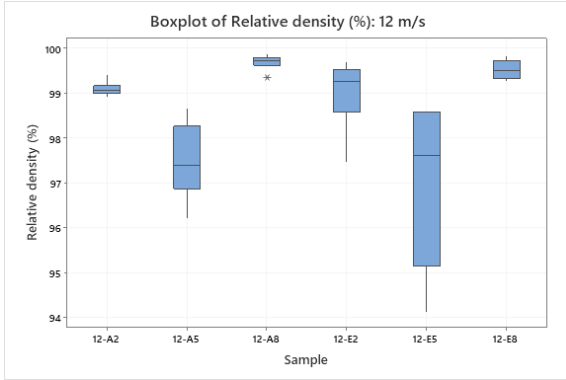
Figure 38: Boxplots of relative density data sets for samples printed at 12 m/s.
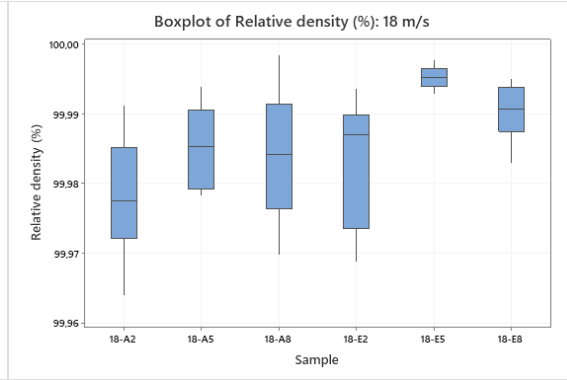
Figure 39: Boxplots of relative density data sets for samples printed at 18 m/s.

A two-sample t-test with 95% confidence interval was carried out to statistically evaluate the relative density of the samples printed at 12 m/s to the samples printed at 18 m/s. The results of the test are shown in Table 9. Each test rejected the null hypothesis, meaning that the porosity and relative density of the samples printed at 12 m/s was significantly different from the samples printed at 18 m/s.

Data set	Sample size	Mean porosity	StDev
12-A2	6	0.9000	0.1705
12-A5	6	2.515	0.846
12-A8	8	0.3059	0.1554
12-E2	8	0.986	0.732
12-E5	6	2.995	1.912
12-E8	6	0.4707	0.2387
18-A2	8	0.02180	0.00870
18-A5	6	0.01468	0.00617
18-A8	8	0.01589	0.00931
18-E2	8	0.01649	0.00917
18-E5	6	0.004717	0.001638
18-E8	6	0.00967	0.00423

Table 8: Descriptive statistics of porosity data sets of microstructure analysis samples.

Test	T-value	DOF	P-value	Null hypothesis
A2: 12 m/s vs. 18 m/s	-12.60	5	< 0.001	Rejected
A5: 12 m/s vs. 18 m/s	-7.24	5	0.001	Rejected
A8: 12 m/s vs. 18 m/s	-5.27	7	0.001	Rejected
E2: 12 m/s vs. 18 m/s	-3.75	7	0.007	Rejected
E5: 12 m/s vs. 18 m/s	-3.83	5	0.012	Rejected
E8: 12 m/s vs. 18 m/s	-4.73	5	0.005	Rejected

Table 9: Two sample t-test comparing means of relative density data sets of samples printed at 12 m/s and 18 m/s.

In the microstructure of the samples printed at 12 m/s gas flow speed, redeposited particles were observed. Figure 40 highlights a large spherical spatter particle ($\approx$80 μm diameter), ejected from the melt pool during the SLM process. The size of the particles corresponds with spatter size distributions found in 316L SLM by Gunenthiram et al. [48], Liu et al. [49] and Obeidi et al. [50]. In the 50x magnified image of the spherical spatter particle in Figure 40, dendrite structures could be observed. Dendrite structures grow as molten metal solidifies, indicating that the particle shown in Figure 40 could be identified as a spatter particle and not as unmelted powder.
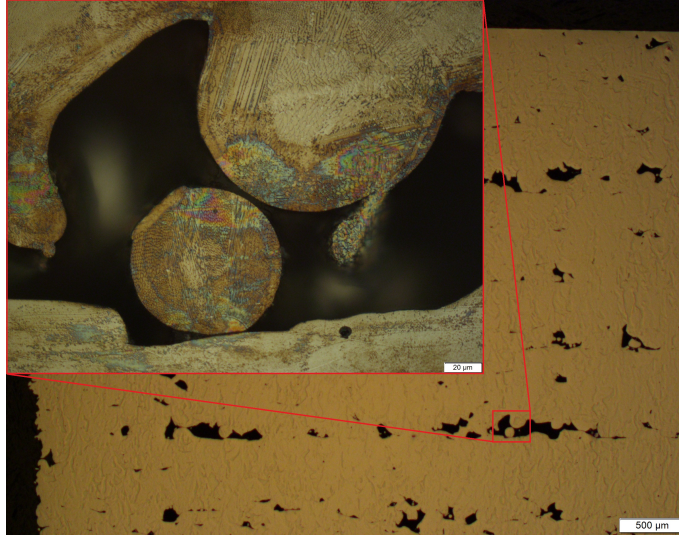

Figure 40: Spatter particles in microstructure of sample A5 printed at 12 m/s. Magnification factor inside red box is 50x. Magnification outside red box is 2.5x.

In Figure 41, the etched microstructure of sample E2 is shown (printed at 12 m/s and 18 m/s). Etching of the samples, conducted using Beraha-I color etchant, made the laser scan tracks visible. In SLM, penetration of the laser melt pool into previous layers creates fusion. Therefore, it would be expected beforehand that laser scan tracks shown in the etched microstructure would show overlap to form a dense metal part. Both microstructures shown in Figure 41 show densely packed scan tracks and layers. No major differences were identified between the etched microstructures of the sample printed at 12 m/s and 18 m/s. However, layers in the 12 m/s microstructure seemed to be slightly less densely packed than in the 18 m/s microstructure. Highlighted in the red boxes in Figure 41a are examples of layers which displayed slightly less overlap. This may be a result of reduced laser power, leading to reduced melt pool penetration depth into the previous layer, and therefore, less overlap between layers. Reduced laser power in the melt pool may be a result of inadequate removal of process by-products from the laser beam. Beam attenuation is directly connected to inert gas flow velocity (Section 2.2.2), which may provide an explanation of the slightly less densely packed microstructure observed in the 12 m/s sample. Additionally, the observation that layers are slightly less densely packed in the 12 m/s could be well-connected to the significant presence of LOF pores in the microstructure. Since overlap between layers creates fusion in the part, insufficient overlap may give rise to lack of fusion.
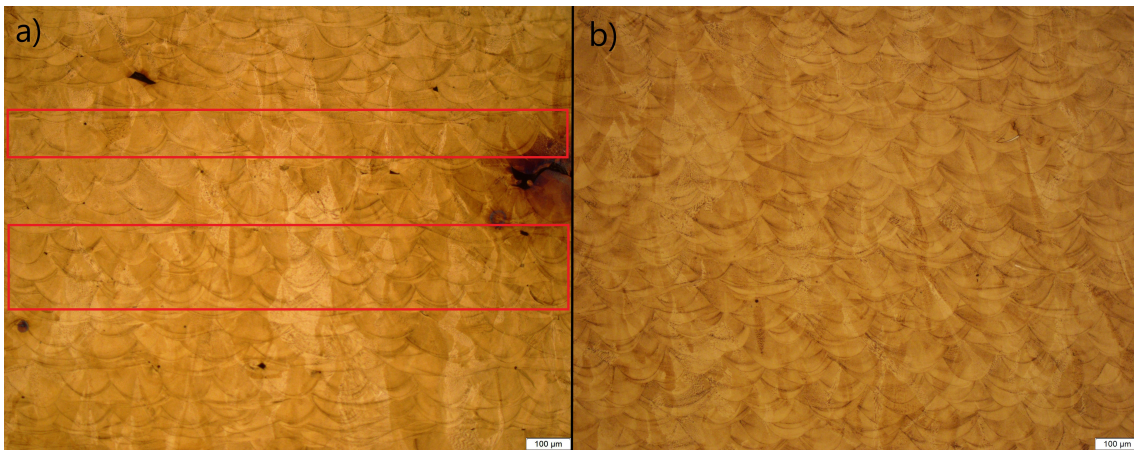

Figure 41: Optical microscopy images of etched samples, magnification factor is 2.5x. Highlighted in the red boxes are layers which show slightly less overlap with adjacent layers. a) Sample E2, printed at 12 m/s, b) Sample E2, printed at 18 m/s.

5.3 Discussion of results

In this section, the results obtained throughout Section 5 are used to answer the research subquestions presented in Section 3.2. The first research subquestion states:

- *How does the inert gas flow behave in the build chamber, and is it uniform across the build plate?*

Flow measurements inside the build chamber, supported by CFD simulations, determined that the flow profile over the build plate is nonuniform in the X- and Y-direction. From inlet to outlet, the magnitude of the flow velocity decreased gradually. The nonuniformity displayed in the Y-direction, perpendicular to the flow, was found to be wave-shaped, with peaks towards the sides of the build plate and a valley over the middle of the build plate. Both flow velocity settings at which data was collected (12 m/s and 18 m/s) displayed similar nonuniform flow profiles over the build plate.

In general, the flow from the inlet jet array and the porous wall was effectively directed to the outlet, with minimal circulation observed in the simulations. However, when flow rate from the porous wall was reduced by 33% (due to blockage of the pores), the desirable behavior of the flow inside the build chamber was no longer maintained. Therefore, preventing the porous wall from significant blockage is an important factor in maintaining desirable flow conditions in the build chamber volume.

- *What is the influence of the inert gas flow on printing quality? Is there a statistical correlation between gas flow velocity and material properties?*

Two main material properties were analyzed in this project: surface roughness and microstructure. During the microstructure analysis, the porosity of the cross-sections was analyzed as well.

Experiment II concluded that the gas flow setting on the SLM 280HL has a significant influence on the surface roughness of the samples. For a sample size of 270 measurements per batch, the mean R_a of the batch printed at 12 m/s was found to be 38.5% higher than the mean R_a of the batch printed at 18 m/s. Similarly, the mean R_z of the batch printed at 12 m/s was found to be 40.3% higher than the mean R_z of the batch printed at 18 m/s. The statistical significance of the results was confirmed using a two-sample t-test ($p<0.001$). Furthermore, intra-build nonuniformity of R_a and R_z was found to be higher in the 12 m/s build. Using a fit regression model, a significant correlation was found between the flow profile over the build plate and the surface roughness profile (R_a and R_z) in the 12 m/s build. In the 18 m/s build, a significant correlation was found between the flow profile over the build plate and the R_z profile.

Microstructure analysis revealed significant lack of fusion in the 12 m/s samples. LOF porosity, caused by insufficient laser energy to melt and fuse the current layer to the previous layer(s), is a phenomenon well-connected to insufficient removal of process by-products [6]. LOF pores were rarely identified within the 18 m/s microstructure. LOF pores are known to initiate cracks, and the effective cross-section of the samples under tensile loading is reduced due to high lack of fusion concentrations between layers. Therefore, it was hypothesized that mechanical performance of the samples printed at 12 m/s was significantly reduced compared to the 18 m/s samples. Delamination, which was observed during the removal of support structures of the 12 m/s samples, supported this hypothesis. Furthermore, the samples printed in front of the middle of the inlet jet array showed the "worst" microstructure, with the largest degree of lack of fusion present and the highest porosity. This could be linked to the flow profile over the build plate, which is lowest in this region. It may be that removal of process by-products under these conditions might be inadequate, causing absorption and scattering of of the laser beam. Porosity analysis was conducted on the microstructure images: The porosity of the samples printed at 12 m/s was found to be almost 100x larger than the porosity of the samples printed at 18 m/s (1.36% at 12 m/s versus 0.0139% at 18 m/s). Finally, the etched microstructure of samples from the batches printed at 12 m/s and 18 m/s were analyzed. Apart from significantly larger porosity in the 12 m/s microstructure, no major differences were found between the etched microstructures of the samples printed at different gas flow velocities. There seemed to be slightly less overlap between layers in the 12 m/s microstructure, which may have been a result of lower penetration depth of the melt pool due to reduced laser power. This may have been caused by interference of process by-products with the laser beam.

6   Conclusion

SLM is a manufacturing method displaying enormous potential in a wide range of applications. ICD-AM investigates this potential within the stakeholders' companies. Over the years, ICD-AM has made much progress in understanding the effects of process parameters on the printing quality of their SLM 280HL machine. During the SLM process, an inert gas is fed through the build chamber to create an inert atmosphere and to transport unfavorable process by-products. In literature, the influence of inert gas flow (velocity) on SLM printing quality is confirmed. However, ICD-AM lacked an understanding of the behavior and influence of the inert gas flow within the SLM 280HL. The work conducted within this MDP provided ICD-AM with a thorough understanding of the inert gas flow behavior during SLM, as well as its influence on surface roughness and microstructure of manufactured parts.

The gas flow behavior in the build chamber was characterized using flow measurements and CFD simulations, at two gas flow velocity settings: 12 m/s and 18 m/s (default parameter). The flow profile over the build plate displayed significant nonuniformity, caused by the nonuniform flow fed into the build chamber through the inlet jet array. Flow conditions throughout the build chamber were found to be desirable under standard conditions. However, when flow rate through the porous wall was reduced due to blockage, these conditions were no longer maintained.

Experimental batches were printed at 12 m/s and 18 m/s gas flow velocity setting to evaluate the influence of varying gas flow velocity on printing quality of the SLM 280HL. Dramatic differences in both surface roughness and microstructure were observed.

The surface roughness of the batch printed at 12 m/s was significantly higher than that of the batch printed at 18 m/s, both for R_a and R_z. Furthermore, the intra-build nonuniformity of the surface roughness was directly linked to the flow profile over the build plate for R_a (12 m/s) and R_z (12 m/s and 18 m/s). Statistical analysis confirmed the significance of aforementioned results, therefore confirming that surface roughness of SLM-manufactured parts is affected by inert gas flow velocity.

Microstructure analysis revealed differences in the 12 m/s and 18 m/s samples. LOF pores, originating from insufficient laser power in the laser melt pool, were present in high concentrations in the 12 m/s samples, whilst being practically absent in the 18 m/s samples. Furthermore, microstructure analysis of the 12 m/s samples revealed redeposited spatter. Spatter particles were not observed in the 18 m/s microstructure. Aforementioned observations could be well-connected to the inadequate transport of process by-products, leading to beam attenuation and

redeposition.

Porosity analysis of the polished sample cross-sections showed significant differences: The average sample porosity of the 12 m/s batch was almost 100x higher than the average porosity of the 18 m/s batch. The 18 m/s samples displayed excellent relative density (>99.95%), confirming that the default gas flow velocity parameter currently used within ICD-AM produces metal parts of high quality.

For the ICD-AM group, the conclusion can be drawn that the inert gas flow at 18 m/s is adequate at transporting process by-products away from the laser beam and powder bed. Surface roughness, microstructure, and porosity of the samples was found to be largely uniform over the build plate, and slight deviations from this uniformity may be attributed to convective cooling of the laser melt pool instead of inadequate removal of process by-products. The significant nonuniformity of the measured flow profile does not seem to be a major problem at the moment. Therefore, no changes to the current SLM 280HL print strategy regarding gas flow are required. However, when ICD-AM engineers start to notice deviations in intra-build quality, the gas flow is a process parameter that should be considered. This MDP proves the significant impact which decreased inert gas flow rate may have on print quality. When the flow profile over the build plate becomes problematic, a redesign of the inlet jet array would be recommended, as the flow from the inlet jet was found to directly determine the flow profile dynamics over the build plate.

In general, this MDP concludes that the inert gas flow velocity is an SLM process parameter which should not be overlooked. Whereas parameters such as laser power and layer thickness are widely studied, studies into the inert gas flow behavior and influence are relatively underrepresented in literature. This MDP concludes the significant impact of a change in the flow velocity parameter of 33%: surface roughness, microstructure, and porosity were all significantly affected. Due to the timeframe of the MDP, it was not feasible to test more material properties, but observation of the samples' microstructure strongly suggested that other material properties, such as mechanical performance, are also directly influenced by the inert gas flow.

7 Master Design Project evaluation

Looking back at the past five months, I can draw the conclusion that I enjoyed working on this project at Philips Drachten. Working within a high-tech, globally respected company provided me a valuable experience at the start of my professional career. Personally, I am pleased with the results of this project. The experiments yielded interesting, statistically significant results. A big motivation for me throughout the project was the genuine interest of co-workers within ICD-AM, who showed great attention in the project's results. In general, the working atmosphere within ICD-AM and Philips Drachten was experienced as very pleasant.

Due to COVID-19, most of the project was conducted from home. Over the course of the project, I got a good impression of the atmosphere within a company environment, but the feeling of a full-time job was never really established. Additionally, communication with co-workers and stakeholders was more time-consuming as most of them were also working from home. More (experimental) work might have fitted into the project's scope if it was conducted full-time at the Philips facility. Furthermore, the ICD-AM group moved to a different building on the Philips facility at the start of February. Therefore, the SLM 280HL was unavailable for several weeks until the end of my MDP at Philips. Initially, the period in which the SLM 280HL would be offline was expected to be shorter. Therefore, the evaluation of internal residual stresses had to be excluded from the project's scope. Luckily, the other experimental results obtained throughout the project were not influenced by the absence of internal residual stresses data.

7.1 Recommendations for future research

Throughout the project, some opportunities for future research and projects were identified:

- Redesign of the lower inlet jet array to improve the flow uniformity over the build plate.

- Microstructure analysis strongly suggested that mechanical properties are also affected by gas flow, which was further supported by delamination in the 12 m/s samples. Mechanical tests, such as tensile tests and fatigue tests, may be conducted to test this hypothesis.

- To monitor porous wall blockage, flow/pressure sensors could be installed in the argon supply piping to the porous wall and the lower inlet jet array.

7.2 Acknowledgements

At the end of this MDP, I would like to thank some of the people without whom the project would not have been possible. I would like to thank Dr. T.C. Pijper, my company supervisor, for providing me with the opportunity to conduct my MDP at Philips Drachten. During the project, he was actively involved and always open for questions, to provide feedback and to help out in general. Dr. M. Muñoz-Arias also provided a lot of helpful feedback throughout the project, especially in the problem definition and research plan phase. Prof. Dr. Y. Pei also provided helpful feedback for the project, as well as the opportunity to conduct flow measurements in the university's SLM machine (SLM 150HL).

Furthermore, I would like to thank my co-workers (W. Slingenbergh, S. van Gerwen, L. Boersma) within ICD-AM for their assistance operating the SLM 280HL and general involvement in the project. Without their help, I would not have been able to perform the measurements and experiments in this project. Finally, I would like to thank M. de Vries for her assistance in the microstructure analysis of the samples and their preparation.

References

[1] O. Abdulhameed & A. Al-Ahmari & W. Ameen & S.H. Mian. Additive manufacturing: Challenges, trends and applications. *Advances in Mechanical Engineering*, 11(2):1–27, 2019.

[2] T.D. Ngo & A. Kashani & G. Imbalzano & K.T.Q. Nguyen & D. Hui. Additive manufacturing (3d printing): A review of materials, methods, applications and challenges. *Composites Part B*, 2018.

[3] H.M. Wang. Materials' fundamental issues of laser additive manufacturing for high-performance large metallic components. *Acta Aeronautica Et Astronautica Sinica*, 35(10):2690–2698, 2014.

[4] F. Caiazzo & F. Cardaropoli & V. Alfieri & V. Sergi & L. Cuccaro. Experimental analysis of selective laser melting process for ti-6al4 v turbine blade manufacturing. In *19th International Symposium on High-Power Laser Systems and Applications (HPLS&A)*, 2012.

[5] C. Yan & L. Hao & A. Hussein & P. Young. Ti6al4 v triply periodic minimal surface structures for bone implants fabricated via selective laser melting. *Journal of the Mechanical Behavior of Biomedical Materials*, 51:61–73, 2015.

[6] A. Ladewig & G. Schlick & V. Fisser & V. Schulze & U. Glatzel. Influence of the shielding gas flow on the removal of process by-products in the selective laser melting process. *Additive Manufacturing*, 10:1–9, 2016.

[7] B. Zhang & Y. Li & Q. Bai. Defect formation mechanisms in selective laser melting: A review. *Chinese Journal of Mechanical Engineering*, 30:515–527, 2017.

[8] W.H. Wu & Y.Q. Yang & K.X. Lai. Process analysis of rapid prototyping with selective laser melting. *Journal of South China University of Technology (Natural Science Edition)*, 3:22–27, 2007.

[9] J.F. Zhao & Z.Y. Ma & D.Q. Xie & X. Han & M. Xiao. Metal additive manufacturing technique. *Journal of Nanjing University of Aeronautics and Astronautics*, 46(5):675–683, 2014.

[10] L. Dowling & J. Kennedy & S. O'Shaughnessy & D. Trimble. A review of critical repeatability and reproducibility issues in powder bed fusion. *Material and Design*, 186, 2020.

[11] B. Ferrar & L. Mullen & E. Jones & R. Stamp & C.J. Sutcliffe. Gas flow effects on selective laser melting (slm) manufacturing performance. *Journal of Materials Processing Technology*, 212(2):355–364, 2012.

[12] D.S. Nguyen & H.S. Park & C.M. Lee. Effect of cleaning gas stream on products in selective laser melting. *Materials and Manufacturing Processes*, 34(4):455–461, 2018.

[13] A.B. Anwar & Q.C. Pham. Study of the spatter distribution on the powder bed during selective laser melting. *Additive Manufacturing*, 22:86–97, 2018.

[14] G. Bean & D.B. Witkin & T.D. McLouth & R. Zaldivar. Process gas influence on microstructure and mechanical behaviour of inconel 718 fabricated via selective laser melting. In *Progress in Additive Manufacturing*, 2020.

[15] Q.C. Liu & J. Elambasseril & S.J. Sun. The effect of manufacturing defects on the fatigue behavior of ti6al4 v specimens fabricated using selective laser melting. *Advanced Materials Research*, 891-892:1519–1524, 2014.

[16] T.G. Spears & S.A. Gold. In-process sensing in selective laser melting (slm) additive manufacturing. *Integrating Materials and Manufacturing Innovation*, 5(2), 2016.

[17] G. Johnson & K. Scholes. *Exploring Corporate Strategy*. Europa, Prentice Hall, 1999.

[18] C. Pauzon & E. Hryha & P. Forêt & L. Nyborg. Effect of argon and nitrogen atmospheres on the properties of stainless steel 316 [U+202F]l parts produced by laser-powder bed fusion. *Materials and Design*, 179(107873), 2019.

[19] M. Velasco-Castro & E. Hernández-Nava & I.A. Figueroa & I. Todd & R. Goodall &. The effect of oxygen pickup during selective laser melting on the microstructure and mechanical properties of ti–6al–4v lattices. *Heliyon*, 5(12), 2019.

[20] R. Li & J. Liu & Y. Shi & L. Wang. Balling behavior of stainless steel and nickel powder during selective laser melting process. *International Journal of Advanced Manufacturing Technology*, 59:1025–1035, 2012.

[21] A. Noskov & T.K. Ervik & I. Tsivilkiy & A. Gilmutdinov & Y. Thomassen. Characterization of ultrafine particles emitted during laser-based additive manufacturing of metal parts. *Scientific Reports*, 10(20989), 2020.

[22] M. Lutter-Günther & M. Bröker & T. Mayer & S. Lizak & C. Seidel & G. Reinhart. Spatter formation during laser beam melting of alsi10mg and effects on powder quality. *Procedia CIRP*, 74:33–38, 2018.

[23] M. Simoncelli & N. Aboulkhair & I. Maskery & C. Tuck & I. Ashcroft & N. Everitt & R. Wildman & R. Hague. Aspects of the process and material relationships in the selective laser melting of aluminium alloys. In *TMS 2015 144th Annual Meeting & Exhibition*, pages 397–404, 2015.

[24] P.Y. Shcheglov & A.V. Gumenyuk & .B. Gornushkin & M. Rethmeier & V.N. Petrovskiy. Vapor-plasma plume investigation during high-power fiber laser welding. *Laser Physics*, 23(1), 2013.

[25] J. Greses & P.A. Hilton & C.Y. Barlow & W.M. Steen. Plume attenuation under high power nd:yttrium-aluminium-garnet laser welding. *Journal of Laser Applications*, 16(9), 2004.

[26] T. Grünberger & R. Domröse. Identification of process phenomena by optical in-process monitoring. *Laser Technik Journal*, 1, 2015.

[27] I. Yadroitsev & I. Yadroitsava & P. Bertrand & I. Smurov. Factor analysis of selective laser melting process parameters and geometrical characteristics of synthesized single tracks. *Rapid Prototyping Journal*, 18(3):201–208, 2012.

[28] H. Gong & K. Rafi & T. Starr & B. Stucker. The effects of processing parameters on defect regularity in ti-6al-4v parts fabricated by selective laser melting and electron beam melting. In *Solid Freeform Fabrication*, 2013.

[29] S.A. Khairallah & A.T. Anderson & A. Rubenchik & W.E. King. Laser powder-bed fusion additive manufacturing: Physics of complex melt flow and formation mechanisms of pores, spatter, and denudation zones. *Acta Materiala*, 108:36–45, 2016.

[30] A. Kidess & S. Kenjeres & B.W. Righolt & C.R. Kleijn. Marangoni driven turbulence in high energy surface melting processes. *International Journal of Thermal Sciences*, 104:412–422, 2016.

[31] V. Gunenthiram & P. Peyre & M. Schneider & M. Dal & F. Coste & R. Fabbro. Analysis of laser-melt pool-powder bed interaction during the selective laser melting of a stainless steel. *Journal of Laser Applications*, 29(2), 2017.

[32] P. Mercelis & J.-P. Kruth. Residual stresses in selective laser sintering and selective laser melting. *Rapid Prototyping Journal*, 12:254–265, 2006.

[33] W. Xing & D. Ouyang & N. Li & L. Liu. Estimation of residual stress in selective laser melting of a zr-based amorphous alloy. *Materials*, 11, 2018.

[34] T. Mishurova & S. Cabeza & K. Artzt & J. Haubrich & M. Klaus & C. Genzel & G. Requena & G. Bruno. An assessment of subsurface residual stresses analysis in slm ti-6al-4v. *Materials*, 10(348), 2017.

[35] F. Rickhey & K.P. Marimuthu & H. Lee. Investigation on indentation cracking-based approaches for residual stress evaluation. *Materials*, 10(404), 2017.

[36] G.T. Doran. There's a s.m.a.r.t. way to write management's goals and objectives. *Management Review*, 70(11):35–36, 1981.

[37] A. Philo & N.P. Lavery & S.G.R. Brown & J. Cherry & J. Sienz & J. Joannou & C.J. Sutcliffe. Comparison and validation of gas flow models in a powder bed selective laser melting process. In *Proceedings of the 23rd UK Conference for Computational Mechanics in Engineering, 8-10 April 2015, Swansea University, Swansea*.

[38] M. Schniedenharn & F. Wiedemann & J.H. Schleifenbaum. Visualization of the shielding gas flow in slm machines by space-resolved thermal anemometry. *Rapid Prototyping Journal*, 24(8):1296–1304, 2018.

[39] Circuit Globe. Hot wire anemometer, 2021.

[40] Y. Chen & V. Guglielmo & Y.W. Zhang. Optimization of inert gas flow inside laser powder bed fusion chamber with computational fluid dynamics. In *Solid Freeform Fabrication 2018: Proceedings of the 29th Annual International Sold Freeform Fabrication Symposium - An Additive Manufacturing Conference*, pages 1931–1939, 2018.

[41] W.-C. Wang & C.-Y. Chang. Flow analysis of the laminated manufacturing system with laser sintering of metal powder. part i: flow uniformity inside the working chamber. *International Journal of Advanced Manufacturing Technology*, 92:1299–1314, 2017.

[42] Additive Manufacturing. The difference between ra and rz, jul 2015.

[43] S. Coeck & M. Bisht & J. Plas & F. Verbist. Prediction of lack of fusion porosity in selective laser melting based on melt pool monitoring data. *Additive Manufacturing*, 25:347–356, 2019.

[44] S.V. Adiban & M. Ramu. Study on the effect of weld defects on fatigue life of structures. In *Materials Today: Proceedings*, volume 5, pages 17114–17124, 2018.

[45] L.L. Parimi & G.A. Rami & D. Clark & M.M. Attallah. Microstructural and texture development in direct laser fabricated in718. *Materials Characterization*, 89:102–111, 2014.

[46] P.K. Neghlani. Slm additive manufacturing of alloy 718 effect of process parameters on microstructure and properties. Master's thesis, University West, Trollhättan, Sweden, 2016.

[47] Inside Metal Additive Manufacturing. Visual guide to the most common defects in powder bed fusion technology, 2016.

[48] V. Gunenthiram & P. Peyre & M. Schneider & M. Dal & F. Coste & I. Koutiri & R. Fabbro. Experimental analysis of spatter generation and melt-pool behavior during the powder bed laser beam melting process. *Journal of Materials Processing Technology*, 251:376–386, 2018.

[49] Y. Liu & Y. Yang & S. Mai & D. Wang & C. Song. Investigation into spatter behavior during selective laser melting of aisi 316l stainless steel powder. *Materials and Design*, 87:797–806, 2015.

[50] M.A. Obeidi & A. Mussatto & R. Groarke & R.K. Vijayaraghavan & A. Cpnway & F.R. Kaschel & E. McCarthy & O. Clarkin & R. O'Connor & D. Brabazon. Comprehensive assessment of spatter material generated during selective laser melting of stainless steel. *Materials Today Communications*, 25, 2020.

[51] The Engineering Toolbox. Gases - dynamic viscosity, 2014.

[52] The Engineering Toolbox. Argon - density and specific weight, 2018.

──────── Appendices ────────

A   Appendix A: COMSOL model specifications

Study setup: A **3D** simulation domain was chosen. For physics, **Turbulent Flow, k-ϵ (spf)** was selected. A **Stationary** study was chosen.

A.1   Parameters and variables

All parameters and variables that were used in the COMSOL model are shown in this section.

Table 10: COMSOL parameters for geometry, material properties and physics

Parameter	Value	Description
T_C	36.05 [K]	Temperature in Celsius
Pbar	12 [mbar]	Overpressure
P_correction	1.02525	Pressure correction factor
Xbc	425 [mm]	Width of build chamber
Ybc	712 [mm]	depth of build chamber
Zbc	385 [mm]	Height of build chamber
Xo_x1	12 [mm]	Depth 1 of outlet notch
Xo_x2	20 [mm]	Depth 2 of outlet notch
Xo_x3	36 [mm]	Depth 3 of outlet notch
Xo_x4	50 [mm]	Depth 4 of outlet notch
Yo	515 [mm]	Width of outlet notch
Zo_big	70 [mm]	Height of big outlet notch
Zo_small	25 [mm]	Height of small outlet notch
Xnotch	70 [mm]	Depth of recoater notch
Znotch_o_low	74 [mm]	Height of recoater notch start (outlet side)
Znotch_o_high	100 [mm]	Height of recoater notch end (outlet side)
Znotch_i_low	68 [mm]	Height of recoater notch start (inlet side)
Znotch_i_high	100 [mm]	Height of recoater notch end (inlet side)
Ypw_low	622 [mm]	Width of porous wall opening (low)
Ypw_middle	684 [mm]	Width of porous wall opening (middle)
Ypw_high	476 [mm]	Width of porous wall opening (high)
Zpw	285 [mm]	Height of porous wall
Zpw_middle	106 [mm]	Height of porous wall (middle)
Zpw_end	46 [mm]	Height of porous wall (end)
Y_door1	12 [mm]	Thickness of door opening

Parameter	Value	Description
Y_door2	16 [mm]	Distance between Y_door1 and start of porous wall opening
Y_inletFull	350 [mm]	Width of full inlet jet array
Y_inletholeFull	5 [mm]	Width of inlet jet and bar
Y_inletbar	1.1 [mm]	Width of inlet bar
Z_inlethole	10 [mm]	Height of inlet jet
Z_inletstart	5[mm]	Height of inlet jet start
XYbp_inner	278 [mm]	Width and depth of build plate substrate
XYbp_outer	280 [mm]	Width and depth of build plate cavity
Rbp_fillet	25 [mm]	Radius of build plate corner fillet
d_backnotch_wall	62 [mm]	Distance between notch in upper rear wall and BC side walls
d_backnotch_roof	5 [mm]	Distance between notch in upper rear wall and BC roof
Y_backnotch	6 [mm]	Depth of notch in upper rear wall
R_backnotch_fillet	3 [mm]	Radius of corner fillet of notch in upper rear wall
X_photostrip	275 [mm]	Width of photostrip
Z_1_photostrip	10 [mm]	Height 1 of photostrip
Z_2_photostrip	38 [mm]	Height 2 of photostrip
Z_3_photostrip	20 [mm]	Height 3 of photostrip
Y_1_photostrip	86 [mm]	Depth 1 of photostrip
Y_2_photostrip	52 [mm]	Depth 2 of photostrip
Y_3_photostrip	32 [mm]	Depth 3 of photostrip

Table 11: COMSOL variables used in model physics

Variable	Expression	Description
T	T_C+273.15 [K]	Temperature in Kelvin

A.2 Geometry

With the measured dimensions, the simulation geometry shown in Figure 42 was built. The recoater (Figure 43) was also included for some simulations to evaluate its effect on flow over the build plate.
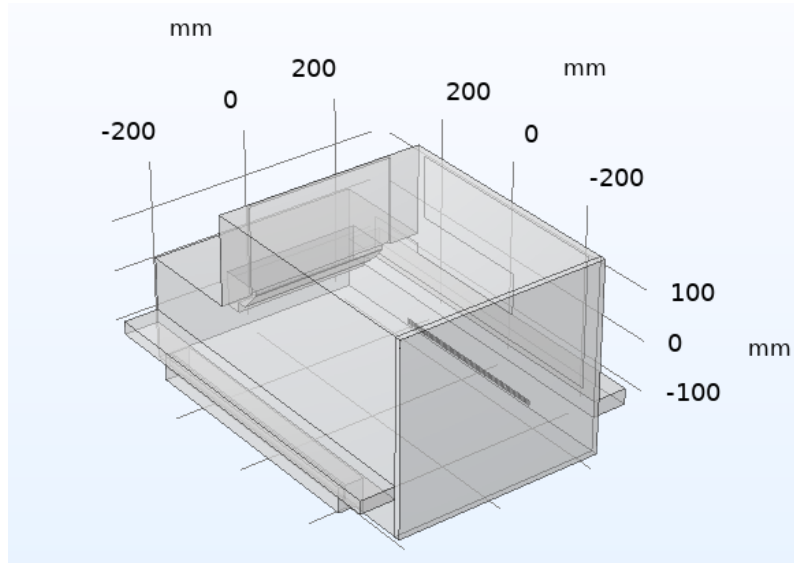
Figure 42: COMSOL geometry resembling SLM 280HL build chamber.
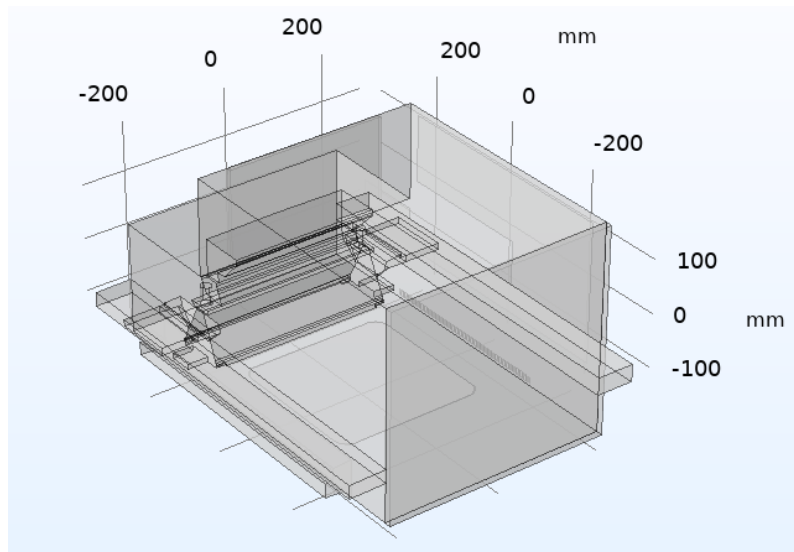

Figure 43: COMSOL geometry resembling SLM 280HL build chamber with recoater in position 1. Position 2 indicates that the recoater is on the other side of the build chamber.

A.3   Materials

Argon gas was assigned to all domains in the model. Material properties for argon (dynamic viscosity [51] and density [52]) with respect to temperature were found in

literature.

Table 12: Argon properties used in COMSOL Multiphysics. Dynamic viscosity (μ) is dependent on gas temperature (Figure 44). Density (ρ) is dependent on temperature (Figure 45) and is corrected for overpressure in the SLM 280HL system (P_correction = 1.02525).

Argon property	Value
Dynamic viscosity (T)	mu(T)
Density (T,p)	P_correction*rho(T)
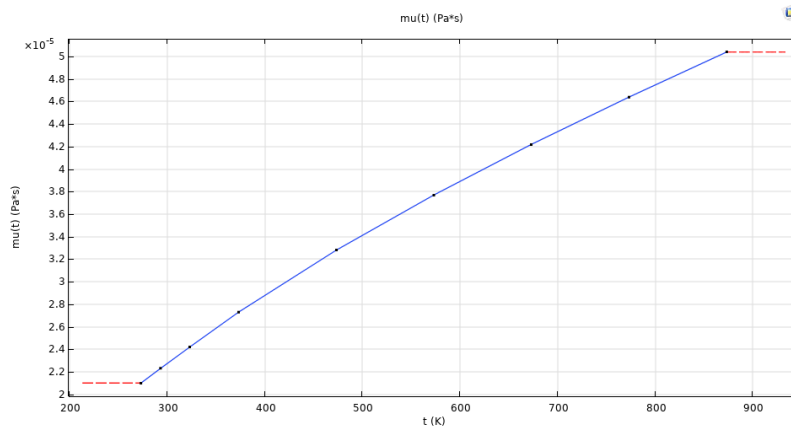
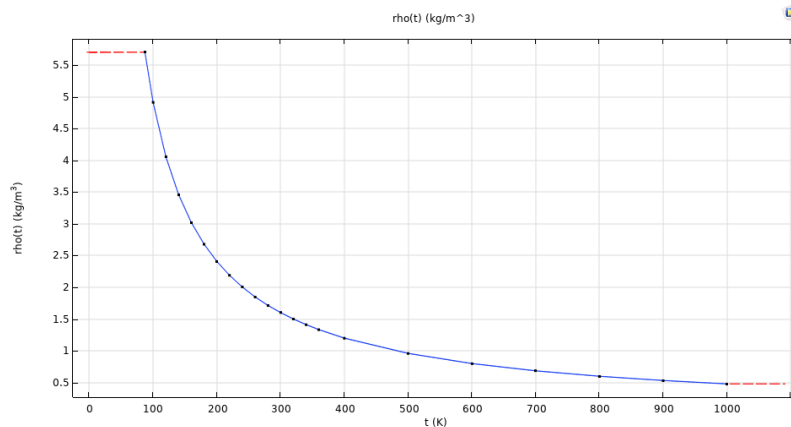Figure 44: Dynamic viscosity (μ) of argon plotted with respect to gas temperature [51]

Figure 45: Density (ρ) of argon plotted with respect to gas temperature. [52]

A.4 Physics

For the inlet jet array and the porous wall (Figure 46), and **Inlet** boundary condition
was chosen. An **Outlet** boundary condition (static pressure = 0 Pa, suppress back-
flow) was assigned to the gas outlet in the build chamber, as can be seen in Figure
47. The **No slip** boundary condition was assigned to all remaining boundaries.
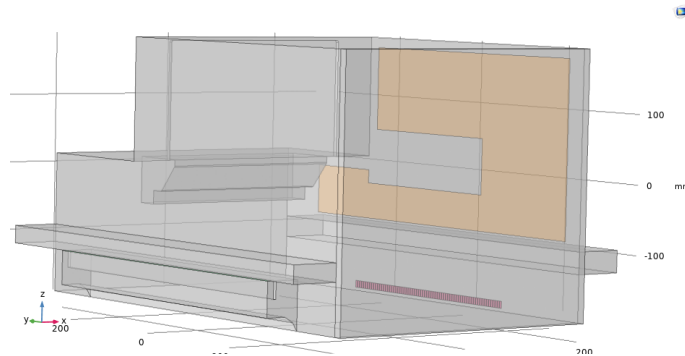

Figure 46: Boundaries with Inlet boundary condition: The inlet jet array
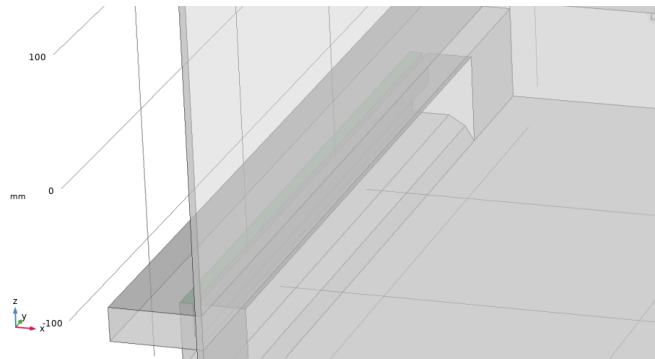(pink) and the porous wall (orange).

Figure 47: Boundary with Outlet boundary condition, shown in lime green.

A.5 Mesh

A **Physics-controlled mesh** with custom adjustments was selected. On default,
COMSOL selects a mesh that is suited to the selected physics (e.g. added boundary
layers for flow physics). The mesh was refined in the domain shown in Figure 48.
For the mesh refinement study, the mesh outside the domain in Figure 48 was set
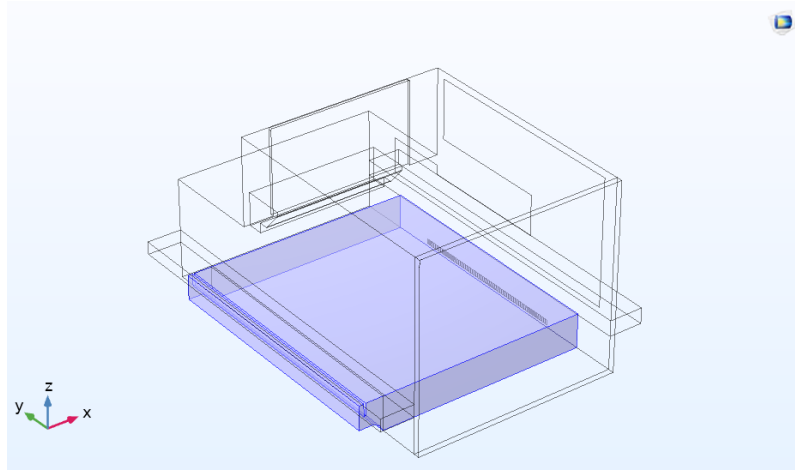to **Coarser** size.

Figure 48: Domain between inlet jet array and outlet in which the mesh was refined. Dimensions of blue domain: x=475 [mm], y=515 [mm], z=70 [mm].

Table 13: Mesh settings for 4.04 maximum element size.

Mesh parameter	Value
Max. element size	4.04 [mm]
Min. element size	0.0933 [mm]
Max. element growth rate	1.02
Curvature factor	0.1
Resolution of narrow regions	1
Mesh outside refinement domain (Figure 48)	
Mesh size outside refinement domain	Physics-controlled: Coarser